

# Forbidden electron capture on $^{24}\text{Na}$ and $^{27}\text{Al}$ in degenerate oxygen-neon cores

D. F. Strömberg,<sup>1,2,3,\*</sup> G. Martínez-Pinedo,<sup>2,1,3,†</sup> and F. Nowacki<sup>4</sup>

<sup>1</sup>*Institut für Kernphysik (Theoriezentrum), Fachbereich Physik,*

*Technische Universität Darmstadt, Schlossgartenstraße 2, 64298 Darmstadt, Germany*

<sup>2</sup>*GSI Helmholtzzentrum für Schwerionenforschung, Planckstraße 1, 64291 Darmstadt, Germany*

<sup>3</sup>*Helmholtz Forschungsakademie Hessen für FAIR,*

*GSI Helmholtzzentrum für Schwerionenforschung, Planckstraße 1, 64291 Darmstadt, Germany*

<sup>4</sup>*Université de Strasbourg, CNRS, IPHC UMR 7178, F-67000 Strasbourg, France*

**Background:** Stars with an initial mass of  $\sim 7$ – $11$  solar masses form degenerate oxygen-neon cores following carbon burning. Electron captures in such cores can trigger runaway oxygen burning, resulting in either a collapse or a thermonuclear explosion. Previous work constrained the contribution of the forbidden  $0_{\text{g.s.}}^+ \rightarrow 2_{\text{g.s.}}^+$  transition to the  $^{20}\text{Ne}(e^-, \nu_e)^{20}\text{F}$  rate and discussed its significance for the evolution of the core.

**Purpose:** We provide a detailed description of the formalism used in previous work and apply it to two further forbidden transitions that are relevant to degenerate oxygen-neon cores: the  $4_{\text{g.s.}}^+ \rightarrow 2_1^+$  transition in  $^{24}\text{Na}(e^-, \nu_e)^{24}\text{Ne}$  and the  $5/2_{\text{g.s.}}^+ \rightarrow 1/2_{\text{g.s.}}^+$  transition in  $^{27}\text{Al}(e^-, \nu_e)^{27}\text{Mg}$ .

**Method:** The relevant nuclear matrix elements are determined through shell model calculations and constraints from CVC theory. We then investigate the astrophysical impact using the stellar evolution code MESA (Modules for Experiment in Stellar Astrophysics) and through timescale arguments.

**Results:** In the relevant temperature range, the forbidden transitions substantially reduce the threshold densities for  $^{24}\text{Na}(e^-, \nu_e)^{24}\text{Ne}$  and  $^{27}\text{Al}(e^-, \nu_e)^{27}\text{Mg}$ . In the MESA models,  $^{24}\text{Na}(e^-, \nu_e)^{24}\text{Ne}$  now occurs immediately following the onset of  $^{24}\text{Mg}(e^-, \nu_e)^{24}\text{Na}$ . The impact on the overall evolution is uncertain: this is due to known difficulties in accounting for convective instabilities triggered by the  $A = 24$  electron captures. The transition between  $^{27}\text{Al}$  and  $^{27}\text{Mg}$  may have a minor effect on the early evolution but is unlikely to affect the outcome.

**Conclusions:** The studied transitions should be included when calculating weak interaction rates between  $^{24}\text{Na}$  and  $^{24}\text{Ne}$  for temperatures  $\log_{10}(T[\text{K}]) \lesssim 8.5$  and between  $^{27}\text{Al}$  and  $^{27}\text{Mg}$  for  $\log_{10}(T[\text{K}]) \lesssim 8.8$ .

## I. INTRODUCTION

Stars with an initial mass of roughly 7 to 11 solar masses ( $M_\odot$ ) form super asymptotic giant branch (Super-AGB) stars following carbon burning [1–3]. Such stars have a degenerate oxygen-neon (ONe) core composed mostly of  $^{16}\text{O}$  and  $^{20}\text{Ne}$ , with minor amounts of other nuclei such as  $^{23}\text{Na}$ ,  $^{24}\text{Mg}$ ,  $^{25}\text{Mg}$ , and  $^{27}\text{Al}$ . Thermal pulses in the surrounding shells add mass to the core and causes it to contract. Eventually it may reach densities where exothermic electron capture processes ignite oxygen burning, triggering a thermal runaway. This event is traditionally known as an electron capture supernova (ECSN) and is believed to result in either a collapse (cECSN) to a neutron star [4, 5] or a thermonuclear explosion (tECSN) with an ONeFe white dwarf remnant [6, 7]. If the growth of the core is too slow the Super-AGB star will expel its envelope before an ECSN occurs. The resulting ONe white dwarf may still reach the threshold density for electron capture by accreting matter from a binary companion. This will lead to either a collapse or a thermonuclear explosion, analogous to the cECSN and tECSN scenarios described above.

The final outcome of an ECSN depends on both the ignition conditions and the physics of the subsequent runaway. In particular, collapse is expected if the central

density at ignition  $\rho_c^{\text{ign}}$  is larger than a critical density  $\rho_c^{\text{crit}}$ . Recent three-dimensional hydrodynamical simulations [7] indicate that  $\rho_c^{\text{crit}} \approx (1 - 2) \times 10^{10} \text{ g cm}^{-3}$  while similar two-dimensional studies [5] suggest that  $\rho_c^{\text{crit}} \approx (7.9 - 8.9) \times 10^9 \text{ g cm}^{-3}$ . Simulations of the evolution of ONe cores up to the point of ignition have shown that  $\rho_c^{\text{ign}}$  is roughly of the order  $\sim 10^{10} \text{ g cm}^{-3}$ , but there is no consensus on whether it exceeds the above given values of  $\rho_c^{\text{crit}}$  [2–4, 8–15]. Substantial uncertainties are related to the role of convection, the precise composition of the core, and the details of the different electron capture processes.

The effect of a given electron capture depends on the mass number  $A$  of the parent nucleus. Capture on odd- $A$  nuclei generally results in an Urca process where cycles of electron capture and  $\beta^-$  decay (e.g.  $^{25}\text{Mg} + e^- \rightarrow ^{25}\text{Na} + \nu_e$  and  $^{25}\text{Na} \rightarrow ^{25}\text{Mg} + e^- + \bar{\nu}_e$ ) cool through neutrino-antineutrino emission. On the other hand, for an even- $A$  parent nucleus the energy threshold for a subsequent capture on the odd- $A$  daughter is typically lower than for the initial capture. This leads to an exothermic double electron capture such as  $^{20}\text{Ne}(e^-, \nu_e)^{20}\text{F}(e^-, \nu_e)^{20}\text{O}$ .

Prior to ignition the electron capture and  $\beta^-$  decay rates are in general determined by a limited number of transitions. This is because the relatively low temperatures ( $kT \lesssim 100 \text{ keV}$ ) ensure that only low-lying excited states are thermally populated. The rate tabulations [16, 17] used historically only took allowed transitions into account. However, in Ref. [18] it was

\* d.fahlinstroemberg@gsi.de

† g.martinez@gsi.de

shown that the second-forbidden non-unique transition ( $\Delta J^\pi = 2^+$ ) between the ground states of  $^{20}\text{Ne}$  and  $^{20}\text{F}$  could have a substantial effect on the capture rate. Ref. [19] constrained the strength of this transition based on a combination of theory and experiment. The astrophysical impact was studied in Ref. [20], which found that the forbidden transition caused a moderate reduction of  $\rho_c^{\text{ign}}$  while simultaneously shifting the point of ignition away from the center of the core.

This paper expands on the work of Ref. [19, 20] by providing a more complete account of the formalism, and by applying it to two further second-forbidden transitions of interest. The first of these is the transition between the  $4_{\text{g.s.}}^+$  ground state in  $^{24}\text{Na}$  and the  $2_1^+$  excited state in  $^{24}\text{Ne}$ . Its possible astrophysical implications has previously been explored in Ref. [15] for various estimates of the transition strength. We also investigate the  $5/2_{\text{g.s.}}^+ \rightarrow 1/2_{\text{g.s.}}^+$  transition between the ground states of  $^{27}\text{Al}$  and  $^{27}\text{Mg}$ : it was ignored in previous studies [2, 21] of electron capture on  $^{27}\text{Al}$  in degenerate ONe cores. In addition to the above two transitions, we also test our approach by computing the previously measured  $4_{\text{g.s.}}^+ \rightarrow 2_1^+$  transition in the  $\beta^-$  decay of  $^{24}\text{Na}$ .

The paper is organized in the following manner: In Section II we introduce the general expressions needed to calculate the weak interaction rates, while we discuss the corresponding nuclear matrix elements in Section III. We then present the calculated rates for the forbidden transitions in Section IV and discuss the astrophysical ramifications in Section V. Finally, we state our conclusions in Section VI.

## II. WEAK INTERACTION RATES

During the evolution leading up to oxygen ignition the core reaches densities and temperatures of the order  $\rho = 10^8\text{--}10^{10} \text{ g cm}^{-3}$  and  $T = 10^7\text{--}10^9 \text{ K}$ . This means that the nuclei are completely ionized and the electrons can be described as a relativistic and degenerate Fermi gas. The weak interaction rates in such a plasma can be calculated as detailed by Fuller, Fowler and Newman in Ref. [22]. To also include the contribution of forbidden transitions we incorporate the formalism of Behrens and Bühring [23–25] in our treatment. We will now present a summary of this approach. The reader can find a more detailed account in Ref. [26].

### A. Key quantities

The temperatures that we encounter are high enough to thermally populate excited nuclear states. Assuming that the nuclei are in thermal equilibrium with the environment the total electron capture or  $\beta^-$  decay rate

is

$$\lambda^{\text{EC}/\beta^-} = \frac{1}{G(Z, A, T)} \sum_{if} (2J_i + 1) \lambda_{if}^{\text{EC}/\beta^-} e^{-E_i/(kT)} \quad (1)$$

where the sum runs over all possible initial  $i$  and final  $f$  states.  $Z$  and  $A$  refer to the atomic and mass numbers of the parent nucleus and the quantity  $G(Z, A, T) = \sum_i (2J_i + 1) e^{-E_i/(kT)}$  is the corresponding partition function.

The partial rates in (1) are given by the expressions

$$\lambda_{if}^{\text{EC}} = \frac{\ln 2}{K} \int_{w_l}^{\infty} C(w) w p_e(q_{if} + w)^2 F(Z, w) \times S_e(w) dw \quad (2a)$$

$$\lambda_{if}^{\beta^-} = \frac{\ln 2}{K} \int_1^{q_{if}} C(w) w p_e(q_{if} - w)^2 F(Z + 1, w) \times [1 - S_e(w)] dw. \quad (2b)$$

From measurements of superallowed decays the value of the constant  $K$  can be constrained to  $K = 6144 \pm 2 \text{ s}$  [27]. The integration variable  $w$  is the electron energy (including the rest mass) in units of  $m_e c^2$ , where  $m_e$  is the electron mass. Similarly,  $p_e = \sqrt{w^2 - 1}$  is the electron momentum in units of  $m_e c$ . We also define  $q_{if}$  as the difference in energy between the final and initial states

$$q_{if} = \frac{Q_{if}}{m_e c^2} = \frac{M_p c^2 - M_d c^2 + E_i - E_f}{m_e c^2}, \quad (3)$$

again in units of  $m_e c^2$ . Here  $M_p$  and  $M_d$  refer to the nuclear masses of the parent and daughter nuclei, whereas  $E_i$  and  $E_f$  are the initial and final excitation energies. For electron capture the lower limit of integration is

$$w_l = \begin{cases} |q_{if}| & \text{if } q_{if} < -1 \\ 1 & \text{if } q_{if} > -1. \end{cases}$$

In this work we only encounter electron capture reactions where  $q_{if} < -1$  and thus  $w_l = -q_{if}$ .

$F(Z, w)$  is the Fermi function that arises from the Coulomb distortion of the electron wave function around the nucleus. Furthermore, the function  $S_e(w)$  describes the energy distribution of the electrons in the degenerate Fermi gas. It is given by the Fermi-Dirac distribution

$$S_e(w) = \frac{1}{\exp\left(\frac{wm_e c^2 - \mu_e}{kT}\right) + 1} \quad (4)$$

with  $\mu_e$  being the electron chemical potential, again including the rest mass. We can determine  $\mu_e$  from the density  $\rho$ , electron fraction  $Y_e$  and temperature  $T$  by solving the equation

$$\rho Y_e = \frac{m_u}{\pi^2} \left(\frac{m_e c}{\hbar}\right)^3 \int_0^\infty (S_e - S_p) p^2 dp \quad (5)$$

where  $m_u$  is the atomic mass unit and  $S_p$  is the positron energy distribution. The latter is like  $S_e$  given by a

Fermi-Dirac distribution (4), but with the opposite sign of the chemical potential (i.e.  $\mu_p = -\mu_e$ ).

All details on the nuclear structure of the involved nuclei are contained in the shape factor  $C(w)$ . For allowed transitions it is constant with respect to  $w$ . Typically we are only interested in Gamow-Teller transitions in which case we have

$$C(w) = g_A^2 \frac{|\langle f | \sum_k \sigma^k t_{\mp}^k | i \rangle|^2}{2J_i + 1}. \quad (6)$$

Here  $g_A = -1.2762(5)$  [28] is the weak axial coupling constant,  $\sigma^k$  is the spin operator and  $t_{\mp}^k$  refers to the isospin lowering and raising operators (corresponding to  $\beta^-$  decay and electron capture, respectively). The summation index  $k$  runs over all  $A$  nucleons.

For second-forbidden non-unique transitions the shape factor depends on  $w$  and is given by an expression involving eight different nuclear matrix elements. We discuss the determination of the matrix elements in Section III and present the full expressions for  $C(w)$  in Appendix A. The dependence on  $w$  of the shape factor is of the form

$$C(w) = a_0 + \frac{a_{-1}}{w} + a_1 w + a_2 w^2 + a_3 w^3 + a_4 w^4. \quad (7)$$

### B. Coulomb corrections

Coulomb interactions between the electrons and ions have a significant impact on the properties of the high-density plasma. As a consequence we must introduce corrections to some of the quantities presented in the preceding section. Here we follow the treatment of Ref. [29, 30].

The most important effect is an increase in the energy difference between nuclei with different charges. Consequently we must replace  $q_{if}$  in (3) with in-medium values according to

$$q_{if}^{\text{EC,med}} = q_{if}^{\text{EC}} - \Delta q_{if}(Z) \quad (8a)$$

$$q_{if}^{\beta^-, \text{med}} = q_{if}^{\beta^-} + \Delta q_{if}(Z + 1). \quad (8b)$$

This translates to a larger energy barrier for electron capture, essentially delaying the onset of capture to higher densities.

A further correction arises due to the fact that the energy of the captured or emitted electron is modified in the presence of the background electron gas. To account for this we replace the electron chemical potential in (4) with

$$\mu_e^{\text{med}} = \mu_e - V_s. \quad (9)$$

We direct the reader to Ref. [29–31] for details on the calculation of  $\Delta q_{if}(Z)$  and  $V_s$ .

### C. Specific heating rates

Under the assumption that the weak interactions are slow compared to the timescale needed to maintain ther-

mal equilibrium the specific heating rates for electron capture and  $\beta^-$  decay can be written

$$\epsilon^{\text{EC}} = \frac{Y}{m_u} \left[ \mu_e + Q_{\text{g.s.}}^{\text{EC}} - \langle E_\nu \rangle^{\text{EC}} \right] \lambda^{\text{EC}} \quad (10a)$$

$$\epsilon^{\beta^-} = \frac{Y}{m_u} \left[ Q_{\text{g.s.}}^{\beta^-} - \mu_e - \langle E_\nu \rangle^{\beta^-} \right] \lambda^{\beta^-}. \quad (10b)$$

Here  $Y$  is the abundance of the parent nucleus and  $m_u$  is the atomic mass unit. Furthermore,  $Q_{\text{g.s.}}$  denotes the energy difference between the ground states of the parent and daughter nuclei (including Coulomb corrections). Note that for the nuclei considered here we have  $Q_{\text{g.s.}}^{\beta^-} = -Q_{\text{g.s.}}^{\text{EC}} > 0$ .  $\langle E_\nu \rangle^{\text{EC}/\beta^-}$  is the average energy of the emitted neutrinos. Finally,  $\mu_e$  is the electron chemical potential without the correction term in (9).

The average neutrino energy is given by the ratio

$$\langle E_\nu \rangle^{\text{EC}/\beta^-} = \frac{\xi^{\text{EC}/\beta^-}}{\lambda^{\text{EC}/\beta^-}} \quad (11)$$

where  $\lambda^{\text{EC}/\beta^-}$  is the reaction rate (1) and  $\xi^{\text{EC}/\beta^-}$  is the rate of energy loss through neutrino emission. The latter is calculated as

$$\xi^{\text{EC}/\beta^-} = \frac{1}{G(Z, A, T)} \sum_{if} (2J_i + 1) \xi_{if}^{\text{EC}/\beta^-} e^{-E_i/(kT)} \quad (12)$$

with the partial neutrino loss rates being

$$\xi_{if}^{\text{EC}} = m_e c^2 \frac{\ln 2}{K} \int_{w_l}^{\infty} C(w) w p_e(q_{if} + w)^3 \times F(Z, w) S_e(w) dw \quad (13a)$$

$$\xi_{if}^{\beta^-} = m_e c^2 \frac{\ln 2}{K} \int_1^{q_{if}} C(w) w p_e(q_{if} - w)^3 \times F(Z + 1, w) [1 - S_e(w)] dw. \quad (13b)$$

Note that we now have one extra power of the neutrino energy compared to (2a) and (2b).

## III. NUCLEAR MATRIX ELEMENTS

### A. Form factor coefficients

The expressions for the shape factor  $C(w)$  contain quantities  ${}^{V/A}F_{KLs}^{(N)}$  known as form factor coefficients. In the impulse approximation they correspond to nuclear matrix elements  ${}^{V/A}\mathfrak{M}_{KLs}^{(N)}$  according to

$${}^V F_{KLs}^{(N)} = (-1)^{K-L} {}^V \mathfrak{M}_{KLs}^{(N)} \quad (14a)$$

$${}^A F_{KLs}^{(N)} = -g_A (-1)^{K-L} {}^A \mathfrak{M}_{KLs}^{(N)}. \quad (14b)$$

Here  $V$  and  $A$  denote vector and axial matrix elements, respectively. Furthermore,  $K$  is the rank of the corresponding spherical tensor operator, which arises by coupling the orbital angular momentum  $L$  and spin  $s$  of the

leptons. The label  $N$  refers to the order in which the coefficients appear when expanding the corresponding form factors in powers of  $qR$ , where  $q$  is the momentum transfer and  $R$  is the nuclear radius.

In the leading order second-forbidden non-unique transitions depend on a total of eight form factor coefficients. These include  $V_{211}^{(0)}$ ,  $V_{220}^{(0)}$ ,  $A_{221}^{(0)}$  and  $A_{321}^{(0)}$ , as well as four further coefficients denoted by  $V_{220}^{(0)}(k_e, 1, 1, 1)$  and  $A_{221}^{(0)}(k_e, 1, 1, 1)$ , where  $k_e = 1, 2$ . The latter differ from  $V_{220}^{(0)}$  and  $A_{221}^{(0)}$  in that the corresponding operators contain an additional factor  $I(k_e, 1, 1, 1; r)$  that modifies their radial dependence. Note that only seven form factor coefficients appeared in Ref. [19]: The reason is that  $A_{321}^{(0)}$  (corresponding to a rank 3 operator) does not satisfy the triangular selection rule for the  $0^+ \rightarrow 2^+$  transition that occurs in  $^{20}\text{Ne}(e^-, \nu_e)^{20}\text{F}$ . This is the opposite of second-forbidden *unique* transitions ( $\Delta J^\pi = 3^+$ ), which only depend on  $A_{321}^{(0)}$ .

We discuss the  $I(k_e, 1, 1, 1; r)$  factors further in Appendix B and list the single-particle matrix elements corresponding to the different form factor coefficients in Appendix C.

## B. Shell model calculations

To determine the nuclear matrix elements we perform shell model calculations in the *sd*-shell valence space using the ANTOINE code [32, 33] and the USDB interaction [34]. In our calculations we assume harmonic oscillator single-particle wave functions. Following the procedure described in Ref. [35] we can relate the nuclear radius  $R$  and oscillator length  $b$  to measurements of the charge mean-square radius  $\langle r^2 \rangle_{\text{exp}}$ . We take the values of the latter from x-ray spectroscopy of muonic atoms [36]. For the mass number  $A = 24$  we then get  $R = 3.947$  fm and  $b = 1.829$  fm, and for  $A = 27$  we have  $R = 3.954$  fm and  $b = 1.808$  fm.

Our choice of valence space means that we ignore all  $2\hbar\omega$  excitations. To account for this we should renormalize the operators in the nuclear matrix elements. The axial matrix elements may also be affected by the fact that the axial current is not conserved in the nuclear medium. Analogous to the approach used for Gamow-Teller and unique forbidden transitions (see e.g. Ref. [37–39]) we attempt to account for both effects by using two different values of the axial coupling constant:  $g_A = -1.276$  (bare) and  $g_A = -1.0$  (quenched). We do not modify the operators contained in the coefficients of the type  $V_{220}^{(0)}$ : these are essentially of the same type as isovector E2 transitions, which are usually not renormalized in shell model calculations. Finally,  $V_{211}^{(0)}$  is a special case which we discuss in the next section.

## C. Constraints from CVC theory

A limitation of our approach is that an *sd*-shell calculation with harmonic oscillator wave functions yields  $V_{211}^{(0)} = 0$  identically. To arrive at a non-zero value of  $V_{211}^{(0)}$  we can instead relate it to  $V_{220}^{(0)}$  via conserved vector current (CVC) theory as described in Ref. [24]. For  $\beta^-$  decay we then have the following relation:

$$V_{211}^{(0)} = -\frac{1}{\sqrt{10}} \left( \frac{E_\gamma}{m_e c^2} \right) R V_{220}^{(0)}. \quad (15)$$

Here  $E_\gamma$  is the energy of the analog E2 gamma decay in the  $\beta^-$  daughter nucleus and  $R$  is the nuclear radius in units of the reduced electron Compton wavelength  $\lambda_e = \hbar/(m_e c)$ . For electron capture the same relation applies but with a positive sign.

In Ref. [19] we further related  $V_{220}^{(0)}$  in the forbidden transition between  $^{20}\text{F}$  and  $^{20}\text{Ne}$  to the experimentally measured strength  $B(E2)$  of the analog gamma decay in  $^{20}\text{Ne}$ . When combined with (15) and the assumption that the ratios  $V_{220}^{(0)}(k_e, 1, 1, 1)/V_{220}^{(0)}$  are well-described by the shell model calculation this allowed us to determine the entire vector contribution. We do not use this method for the forbidden transitions between  $^{24}\text{Na}$  and  $^{24}\text{Ne}$  or  $^{27}\text{Al}$  and  $^{27}\text{Mg}$  as the corresponding  $B(E2)$  strengths are poorly constrained. In addition, in the  $^{24}\text{Na}(e^-, \nu_e)^{24}\text{Ne}$  case the axial contribution appears to play a more important role than for the forbidden transition in  $^{20}\text{Ne}(e^-, \nu_e)^{20}\text{F}$ . This means that determining the exact magnitude of the vector form factor coefficients may not be as helpful in constraining the electron capture rate.

## IV. CALCULATED RATES

### A. $^{24}\text{Mg} \leftrightarrow ^{24}\text{Na}$

Apart from the forbidden decay of  $^{20}\text{F}$  studied in Ref. [19], there is only one [40] experimentally measured second-forbidden non-unique transition among nuclei with  $A < 36$ : the  $4_{\text{g.s.}}^+ \rightarrow 2_1^+$  transition in the  $\beta^-$  decay of  $^{24}\text{Na}$ . We have calculated the corresponding form factor coefficients as presented in Table I. There are two sets of values: one (SM) taken directly from our shell model calculations and one (SM+CVC) where we have determined  $V_{211}^{(0)}$  via the CVC relation (15). When applying (15) we used the value  $E_\gamma = 8.148$  MeV, which we deduced from the energy level data in Ref. [41]. For this particular transition  $A_{321}^{(0)}$  is several times larger than the other form factor coefficients. However, this does not necessarily mean that it is several times more important in determining the decay rate: the impact of a form factor coefficient also depends on the factors multiplied by it in the expression for the shape factor  $C(w)$ .

TABLE I. Form factor coefficients for the forbidden transition from the  $4_{\text{g.s.}}^+$  state in  $^{24}\text{Na}$  to the  $2_1^+$  state in  $^{24}\text{Mg}$ . These values have been computed assuming  $g_A = -1.276$ .

Form factor coefficient	SM	SM+CVC
$V_{211}^{(0)}$	0	0.00144 <sup>a</sup>
$V_{220}^{(0)}$	-0.0279	-0.0279
$V_{220}^{(0)}(1, 1, 1, 1)$	-0.0352	-0.0352
$V_{220}^{(0)}(2, 1, 1, 1)$	-0.0339	-0.0339
$A_{221}^{(0)}$	-0.0361	-0.0361
$A_{221}^{(0)}(1, 1, 1, 1)$	-0.0452	-0.0452
$A_{221}^{(0)}(2, 1, 1, 1)$	-0.0435	-0.0435
$A_{321}^{(0)}$	-0.121	-0.121

<sup>a</sup> Calculated from  $V_{220}^{(0)}$  via the CVC relation.

TABLE II.  $\log ft$  values calculated from Table I, with and without quenching of the axial form factor coefficients, compared with the experimental value given in Ref. [42].

Form factor coefficients	$g_A$	$\log ft$
SM	-1.276	12.24
SM	-1.0	12.39
SM+CVC	-1.276	12.48
SM+CVC	-1.0	12.68
Exp.	-	12.7

From the form factor coefficients and the resulting  $\beta^-$  decay shape factors  $C(w)$  we have calculated the  $\log(ft)$  values listed in Table II. Our theoretical results can be compared with the measurement  $\log(ft) = 12.7$  given in Ref. [42]. (Note that Ref. [41] also lists the value  $\log(ft) = 11.34$ : this is based on intensity balance arguments and not on any direct measurements.) To arrive at the total forbidden decay rate in Ref. [42] the authors had to extrapolate from the observed region of the electron energy spectrum. In doing so, they effectively assumed that the spectrum was shaped like that of an allowed transition. By their own estimate the transition may in reality be a factor two weaker, giving  $\log(ft) = 13$ .

The results in Table II indicate that we overestimate the transition strength by a factor  $\sim 1$ –3. Comparing with  $\log(ft) = 13$ , we instead get a factor  $\sim 2$ –6. The agreement is better using the non-zero value of  $V_{211}^{(0)}$  given by the CVC relation, and the quenched axial contribution. Compared with previous calculations for second-forbidden *unique* transitions, where shell-model calculations in the *sd*-shell generally predict half-lives that are within a factor two experiment [37, 38], we seem to do somewhat worse. This is related to the complicated interferences between different matrix elements. However, the astrophysical scenarios studied in this work do not appear to be very sensitive to the exact strength of the forbidden transitions: as we shall see in Section V rates that differ by a factor 2–3 produce very similar results.

## B. $^{24}\text{Na} \leftrightarrow ^{24}\text{Ne}$

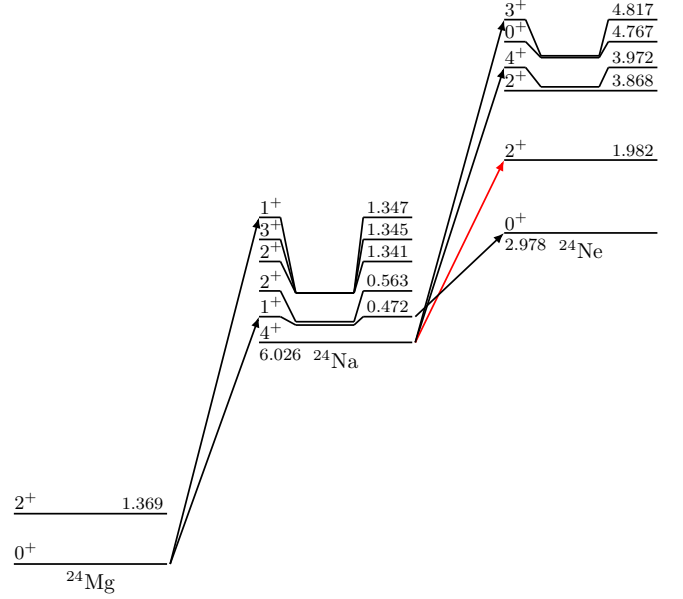


FIG. 1. Energy level diagram illustrating the  $^{24}\text{Mg}(e^-, \nu_e)^{24}\text{Na}(e^-, \nu_e)^{24}\text{Ne}$  double electron capture. We list excitation energies and, for  $^{24}\text{Na}$  and  $^{24}\text{Ne}$ , the ground state energy relative to the ground state of the parent nucleus. All energies are in units of MeV. The nuclear data has been taken from Ref. [18, 41]. Relevant transitions are shown with arrows, with the forbidden transition in red.

We illustrate the transitions relevant to the  $^{24}\text{Mg}(e^-, \nu_e)^{24}\text{Na}(e^-, \nu_e)^{24}\text{Ne}$  double electron capture in Fig. 1. As the transitions between the ground states are fourth forbidden ( $\Delta J^\pi = 4^+$ ) they are too weak to produce any significant electron capture rate. Instead, the  $^{24}\text{Mg}(e^-, \nu_e)^{24}\text{Na}$  reaction proceeds via the allowed  $0_{\text{g.s.}}^+ \rightarrow 1_1^+$  transition to the first excited state in  $^{24}\text{Na}$  at 0.472 MeV. A subsequent  $^{24}\text{Na}(e^-, \nu_e)^{24}\text{Ne}$  capture can then occur through  $1_1^+ \rightarrow 0_{\text{g.s.}}^+$ . Note that the reverse  $\beta^-$  decay rate is Pauli blocked: since  $\mu_e$  is at this point substantially larger than the maximal electron energy, the factor  $[1 - S_e(w)]$  in (2b) vanishes in the interval of integration.

The situation is quite different if the temperature is so low that the population of the  $1_1^+$  state becomes negligible. In this case the rate of the  $^{24}\text{Na}(e^-, \nu_e)^{24}\text{Ne}$  capture is determined by the two transitions  $4_{\text{g.s.}}^+ \rightarrow 2_1^+$  (second forbidden) and  $4_{\text{g.s.}}^+ \rightarrow 4_1^+$  (allowed). Note that the energy threshold of the latter ( $\sim 6.95$  MeV) is slightly higher than for the initial capture on  $^{24}\text{Mg}$  ( $\sim 6.59$  MeV). This means that ignoring the forbidden transition we at low temperatures expect to see two separate capture reactions: first  $^{24}\text{Mg}(e^-, \nu_e)^{24}\text{Na}$  and then  $^{24}\text{Na}(e^-, \nu_e)^{24}\text{Ne}$  at slightly higher densities.

Both of the above reactions are exothermic, i.e. the specific heating rate  $\epsilon^{\text{EC}}$  is positive. For

$^{24}\text{Mg}(e^-, \nu_e)^{24}\text{Na}$  this is due to the capture being delayed until the threshold for the allowed  $0_{\text{g.s.}}^+ \rightarrow 1_1^+$  transition is reached. At this point we have (see Ref. [18])  $\mu_e \approx -Q_{\text{g.s.}}^{\text{EC}} + E_{1+}$  and  $\langle E_\nu \rangle^{\text{EC}} \approx 0$ , where  $E_{1+} = 0.472$  MeV is the excitation energy of the  $1_1^+$  state. When inserted into (10a) the above yields

$$\dot{\epsilon}^{\text{EC}} \approx \frac{Y}{m_u} \lambda_{0^+ \rightarrow 1^+}^{\text{EC}} E_{1+} \quad (16)$$

which we can interpret as the heating arising from the gamma decay of the  $1_1^+$  state. Similarly, if the  $^{24}\text{Na}(e^-, \nu_e)^{24}\text{Ne}$  capture proceeds via the  $4_{\text{g.s.}}^+ \rightarrow 4_1^+$  transition there is an associated heating effect due to the subsequent gamma decay of the excited  $4_1^+$  state. The situation is somewhat different if electron capture instead occurs via the  $1_1^+ \rightarrow 0_{\text{g.s.}}^+$  or  $4_{\text{g.s.}}^+ \rightarrow 2_1^+$  transitions, whose energy thresholds are lower than for the preceding  $^{24}\text{Mg}(e^-, \nu_e)^{24}\text{Na}$  reaction. For such superthreshold captures we naturally have  $\mu_e + Q_{\text{g.s.}} > 0$  but also  $\langle E_\nu \rangle^{\text{EC}} > 0$ . The net effect is, however, still exothermic.

A subtlety in the evaluation of the  $^{24}\text{Na}(e^-, \nu_e)^{24}\text{Ne}$  rate is the fact that the  $1_1^+$  state in  $^{24}\text{Na}$  is an isomer. It decays to the  $4_{\text{g.s.}}^+$  ground state via an M3 transition with a half-life of 20.18 ms [41]. As this is many orders of magnitude slower than typical gamma decays one might ask whether the population of the  $1_1^+$  state still follows a Boltzmann distribution as assumed in (1). In Appendix D we argue that this assumption is still appropriate.

To determine the effect of the forbidden transition on the electron capture rate we have calculated the corresponding form factor coefficients as listed in Table III. In contrast to the preceding section, here we list the form factor coefficients in the electron capture direction. As before we either let  $^VF_{211}^{(0)} = 0$  (SM) or use (15) to relate it to  $^VF_{220}^{(0)}$  (SM+CVC). Since there is no experimental value for  $E_\gamma$  in (15), i.e. the excitation energy of the isobaric analog of the  $^{24}\text{Ne } 2_1^+$  state in  $^{24}\text{Na}$ , we estimate it based on the Coulomb displacement energies between isobaric analog states [43]:

$$E_\gamma = Q + \Delta E_C - (m_n c^2 - m_p c^2), \quad (17a)$$

$$\Delta E_C = 1.4136(1) \bar{Z}/A^{1/3} - 0.91338(11) \text{ MeV} \quad (17b)$$

Here  $Q = 4.959$  MeV is the energy difference between the initial and final states in the forbidden transition, and  $m_n$  and  $m_p$  are the neutron and proton masses. We have also introduced the quantity  $\bar{Z} = (Z_i + Z_f)/2$ . The above equations yield  $E_\gamma = 7.90$  MeV.

From Table III we can derive the corresponding electron capture shape factors, which are trivially related to the ones of the reverse  $\beta^-$  decay (see Appendix A). To give an indication of the transition strength we list the predicted  $\log ft$  values for the  $\beta^-$  decay in Table IV. In addition to the SM and SM+CVC results we also include the values obtained using quenched axial matrix elements. We should note that a lower  $\log(ft)$  value

TABLE III. Form factor coefficients for the forbidden transition from the  $4_{\text{g.s.}}^+$  state in  $^{24}\text{Na}$  to the  $2_1^+$  state in  $^{24}\text{Ne}$ . We use  $g_A = -1.276$  when computing the axial coefficients.

Form factor coefficient	SM	SM+CVC
$^VF_{211}^{(0)}$	0	0.00225 <sup>a</sup>
$^VF_{220}^{(0)}$	0.0451	0.0451
$^VF_{220}^{(0)}(1, 1, 1, 1)$	0.0630	0.0630
$^VF_{220}^{(0)}(2, 1, 1, 1)$	0.0620	0.0620
$^AF_{221}^{(0)}$	-0.109	-0.109
$^AF_{221}^{(0)}(1, 1, 1, 1)$	-0.128	-0.128
$^AF_{221}^{(0)}(2, 1, 1, 1)$	-0.122	-0.122
$^AF_{321}^{(0)}$	-0.00020	-0.00020

<sup>a</sup> Calculated from  $^VF_{220}^{(0)}$  via the CVC relation.

TABLE IV.  $\log ft$  values for laboratory  $\beta^-$  decay corresponding to the form factor coefficients in Table III, with and without quenching applied to the axial coefficients.

Form factor coefficients	$g_A$	$\log ft$
SM	-1.276	11.57
SM	-1.0	11.69
SM+CVC	-1.276	12.14
SM+CVC	-1.0	12.38

does not always imply a higher electron capture rate: the  $\beta^-$  decay rate is determined by the behaviour of the shape factor for electron energies below  $Q^{\beta^-}$ , while electron capture occurs for energies above this value.

We have evaluated the forbidden electron capture rate for both the SM and SM+CVC cases as shown in Fig. 2. To calculate the allowed rates in the plot we used the transition strengths listed in Ref. [18]. In the relevant density range (roughly  $\log_{10}(\rho Y_e [\text{g cm}^{-3}]) = 9.3\text{--}9.4$ ) the SM rate is 2.5–3 times higher than the SM+CVC rate. Quenching of the axial matrix elements results in rates (not shown in the figure) that are 30% to 50% lower. In the upper panel of Fig. 2 we have assumed a temperature of  $\log_{10}(T[\text{K}]) = 8.4$ , which is roughly what is seen in simulations without Urca cooling (see Ref. [14]). In this case the forbidden transition increases the rate by up to 3 orders of magnitude for  $\log_{10}(\rho Y_e [\text{g cm}^{-3}]) \lesssim 9.4$ , but even without this contribution there would still be a substantial capture rate at low densities via the  $1^+ \rightarrow 0^+$  transition. This is not the case in the lower panel, where we have plotted the rates for the temperature  $\log_{10}(T[\text{K}]) = 7.8$ . Such low temperatures are seen in models with substantial Urca cooling (see Ref. [15]). The population of the  $1^+$  state in  $^{24}\text{Na}$  is now so low that the contribution from the  $1^+ \rightarrow 0^+$  transition is negligible and we would see no electron capture for  $\log_{10}(\rho Y_e [\text{g cm}^{-3}]) \lesssim 9.4$  if we did not include the forbidden transition. In general, the forbidden transition will have a significant contribution to the total capture

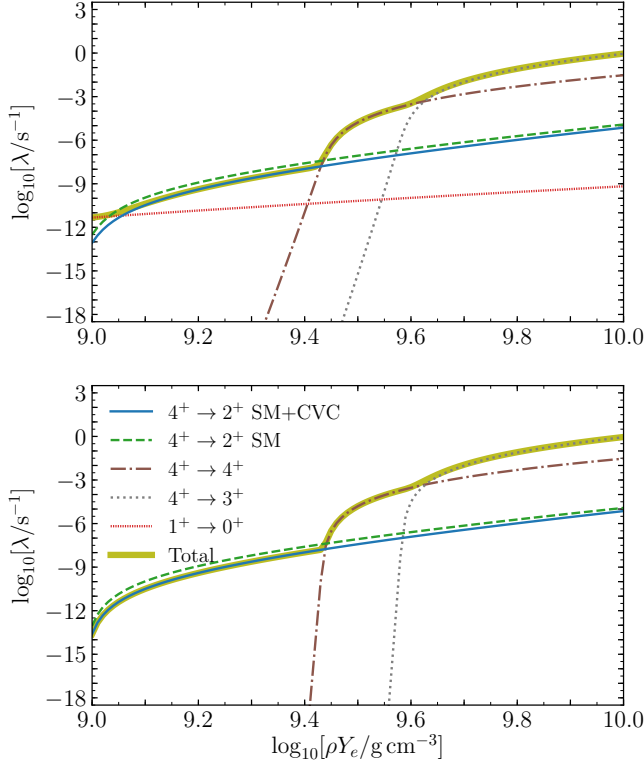


FIG. 2. Electron capture rate on  $^{24}\text{Na}$  as a function of density with Coulomb corrections included. We plot the total rate as well as the individual contributions from the four transitions that dominate the capture rate. The upper panel corresponds to  $\log_{10}(T[\text{K}]) = 8.4$  and the lower panel to  $\log_{10}(T[\text{K}]) = 7.8$ .

rate for temperatures  $\log_{10}(T[\text{K}]) \lesssim 8.5$ .

### C. $^{27}\text{Al} \leftrightarrow ^{27}\text{Mg}$

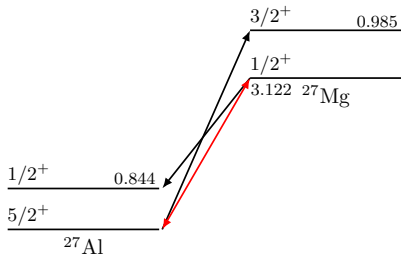


FIG. 3. Energy level diagram illustrating the transitions that determine the rate of the  $^{27}\text{Al}(e^-, \nu_e)^{27}\text{Mg}$  electron capture as well as the reverse beta decay. The forbidden transition is in red. We list excitation energies as well as the ground state energy of  $^{27}\text{Mg}$  relative to the ground state of  $^{27}\text{Al}$ . Both are in units of MeV. The nuclear data has been taken from Ref. [44].

In Fig. 3 we show the transitions that determine the

$^{27}\text{Al}(e^-, \nu_e)^{27}\text{Mg}$  electron capture rate as well as the rate of the reverse  $\beta^-$  decay. As  $^{27}\text{Al}$  and  $^{27}\text{Mg}$  are odd-even nuclei we would expect electron capture to trigger an Urca process. However, at low temperatures this can only occur via the second-forbidden transition between the two ground states. If we instead only consider allowed transitions electron capture is delayed until the threshold for the  $5/2_{\text{g.s.}}^+ \rightarrow 3/2_1^+$  transition is reached. At this point the reverse  $\beta^-$  decay rate of  $^{27}\text{Mg}$  is negligible: there is no significant thermal population of the excited  $3/2^+$  state and the  $1/2_{\text{g.s.}}^+ \rightarrow 1/2_1^+$  transition from the ground state to the first excited state in  $^{27}\text{Al}$  has become Pauli blocked. Without  $\beta^-$  decay there cannot be any Urca cycles and instead of a cooling effect we would see heating from the gamma decay of the excited  $3/2^+$  state (see our discussion in the preceding section). Note that at higher temperatures ( $\log_{10}(T[\text{K}]) \gtrsim 8.8$ ) Urca processes can occur via allowed transitions between excited states. This is demonstrated in Ref. [21], which did not include any forbidden transitions.

To establish whether any significant Urca cooling occurs via the forbidden transition between the ground states we must first constrain its strength. Following the same procedure as in the preceding sections we have calculated the form factor coefficients using shell model (SM) calculations and by also applying the CVC relation (15) (SM+CVC), where we used  $E_\gamma = 6.814$  MeV [44] for the latter. We list the results in Table V. From these coefficients (with and without quenching of the axial part) we derive the corresponding shape factors. We show the resulting  $\log ft$  values of the reverse  $\beta^-$  decay in Table VI.

TABLE V. Form factor coefficients for the forbidden transition from the  $5/2_{\text{g.s.}}^+$  state in  $^{27}\text{Al}$  to the  $1/2_{\text{g.s.}}^+$  state in  $^{27}\text{Mg}$ . For the axial coefficients we assumed  $g_A = -1.276$ .

Form factor coefficient	SM	SM+CVC
$V F_{211}^{(0)}$	0	0.0116 <sup>a</sup>
$V F_{220}^{(0)}$	0.269	0.269
$V F_{220}^{(0)}(1, 1, 1, 1)$	0.316	0.316
$V F_{220}^{(0)}(2, 1, 1, 1)$	0.300	0.300
$A F_{221}^{(0)}$	0.125	0.125
$A F_{221}^{(0)}(1, 1, 1, 1)$	0.139	0.139
$A F_{221}^{(0)}(2, 1, 1, 1)$	0.130	0.130
$A F_{321}^{(0)}$	-0.368	-0.368

<sup>a</sup> Calculated from  $V F_{220}^{(0)}$  via the CVC relation.

In Fig. 4 we plot the electron capture and  $\beta^-$  decay rates as a function of the density at a temperature of  $\log_{10}(T[\text{K}]) = 8.3$ . For the allowed transition between the  $5/2_{\text{g.s.}}^+$  and  $3/2_1^+$  states we used a transition strength corresponding to  $\log ft = 5.51$  in the  $\beta^-$  decay direction. We determined this value through a shell model calculation. As seen in the upper panel we are able to reproduce the rate from Ref. [21] by solely including allowed transitions. Per our earlier discussion there is no

TABLE VI.  $\log ft$  values for laboratory  $\beta^-$  decay corresponding to the form factor coefficients in Table V, with and without quenching applied to the axial coefficients.

Form factor coefficients	$g_A$	$\log ft$
SM	-1.276	11.33
SM	-1.0	11.32
SM+CVC	-1.276	11.13
SM+CVC	-1.0	11.23

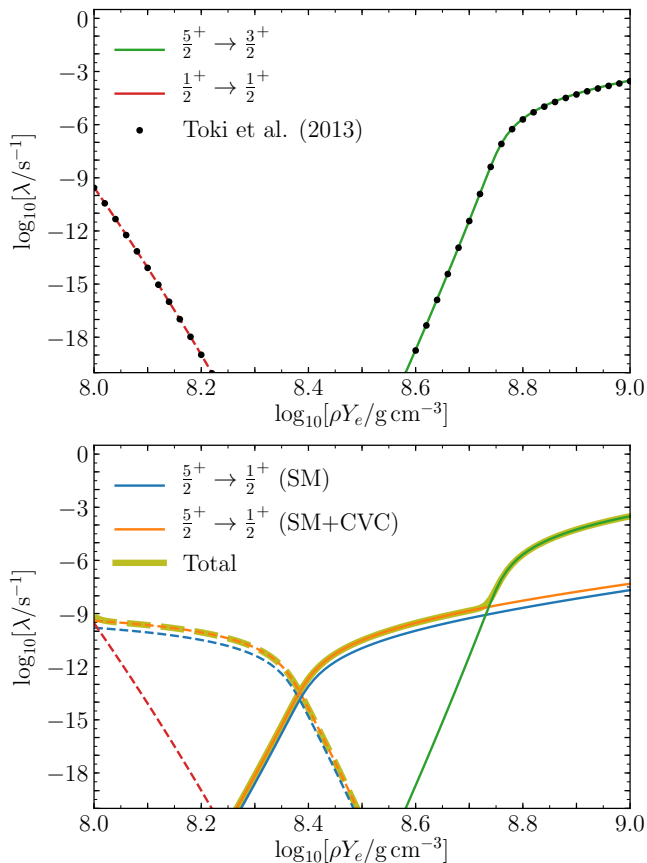


FIG. 4. Electron capture rates on  $^{27}\text{Al}$  (solid) and the reverse  $\beta^-$  decay rates of  $^{27}\text{Mg}$  (dashed) as a function of density with Coulomb corrections included. We have assumed a temperature of  $\log_{10}(T[\text{K}]) = 8.3$ . In the upper panel we only include allowed transitions: this reproduces the rate from Ref. [21]. In the lower panel we show the impact of the forbidden transition. Note that the total electron capture and  $\beta^-$  decay rates are plotted assuming the SM+CVC rate.

Urca cooling in this case: excited states are not thermally populated at this temperature and the  $\beta^-$  decay of the  $^{27}\text{Mg}$  ground state becomes Pauli blocked before electron capture on  $^{27}\text{Al}$  can occur. In contrast, in the lower panel we also include the contribution from the forbidden transition. This significantly alters both the electron capture and  $\beta^-$  decay rates and the density ranges in which the two processes occur now overlap. The decay and capture

rates become roughly equal at  $\log_{10}(\rho Y_e [\text{g cm}^{-3}]) \approx 8.4$ . This is when we would expect the Urca process to be the most efficient. However, at this point the rates are only of the order  $10^{-14} - 10^{-13} \text{ s}^{-1}$ . As a consequence, the Urca cooling is marginal in our models (see Section VB). Nevertheless, the forbidden transition has a large impact on both  $\beta^-$  decay and electron capture rates at temperatures  $\log_{10}(T[\text{K}]) \lesssim 8.8$ , and we recommend its inclusion in stellar evolution modeling.

## V. ASTROPHYSICAL IMPACT

### A. $^{24}\text{Na} \leftrightarrow ^{24}\text{Ne}$

To illustrate the impact of the forbidden transition between  $^{24}\text{Na}$  and  $^{24}\text{Ne}$  we use the one-dimensional stellar evolution code MESA [45] (Modules for Experiments in Stellar Astrophysics, version 10398). We use MESA's ability to calculate weak interaction rates on the fly, which we have extended to support second-forbidden transitions as described in Appendix E.

In our simulations we use the set up of Refs. [14, 15] to which we refer the reader for the full details. In short, a degenerate ONe core is prepared at a density of  $\rho = 0.40 \times 10^9 \text{ g cm}^{-3}$  and mass is then added at a constant rate  $\dot{M}$  to simulate the core growth. For the initial composition we assume the default set of mass fractions used in Ref. [15]:  $X(^{16}\text{O}) = 0.50$ ,  $X(^{20}\text{Ne}) = 0.39$ ,  $X(^{23}\text{Na}) = 0.05$ ,  $X(^{24}\text{Mg}) = 0.05$  and  $X(^{25}\text{Mg}) = 0.01$ . Furthermore, for the growth rate we use the values  $\dot{M} = 10^{-7} \text{ M}_{\odot} \text{ yr}^{-1}$ ,  $10^{-6} \text{ M}_{\odot} \text{ yr}^{-1}$  or  $10^{-5} \text{ M}_{\odot} \text{ yr}^{-1}$ . This is in line with simulations of thermally stable hydrogen and helium burning which predict core growth rates  $(4-7) \times 10^{-7} \text{ M}_{\odot} \text{ yr}^{-1}$  [46] and  $(1.5-4.5) \times 10^{-6} \text{ M}_{\odot} \text{ yr}^{-1}$  [47], respectively.

In Fig. 5 we show the evolution of the central temperature and density for the MESA simulations with the growth rate  $\dot{M} = 10^{-6} \text{ M}_{\odot} \text{ yr}^{-1}$ . The initial evolution is identical, with substantial cooling from the  $^{25}\text{Mg} \leftrightarrow ^{25}\text{Na}$  and  $^{23}\text{Na} \leftrightarrow ^{23}\text{Ne}$  Urca cycles. Differences between the simulations appear once the threshold density for capture on  $^{24}\text{Mg}$  is reached. If the forbidden transition is ignored capture occurs first on  $^{24}\text{Mg}$  and later on  $^{24}\text{Na}$ , as explained in Section IV B. If it is included we get the double electron capture  $^{24}\text{Mg}(e^-, \nu_e)^{24}\text{Na}(e^-, \nu_e)^{24}\text{Ne}$  when the electron chemical potential reaches the threshold for capture on  $^{24}\text{Mg}$ . The difference between using the SM and SM+CVC rates is minimal. Furthermore, the simulations converge for densities  $\rho_c \approx 6 \times 10^9$  independently of the inclusion of the forbidden transition. As explained in Ref. [15] this is due to the core returning to the trajectory defined by the balance between compressional heating and losses from thermal neutrinos.

The subsequent evolution follows the results presented in Ref. [20]: Electron capture on  $^{20}\text{Ne}$  sets in at  $\rho_c \approx 6.8 \times 10^9 \text{ g cm}^{-3}$  via the second-forbidden transition between the ground states of  $^{20}\text{Ne}$  and  $^{20}\text{F}$ . As the

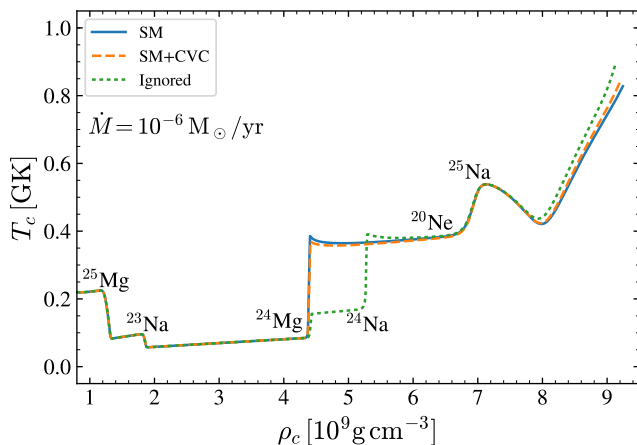


FIG. 5. Central temperature as a function of central density in MESA simulations with three different treatments of the forbidden transition between  $^{24}\text{Na}$  and  $^{24}\text{Ne}$ : included using the SM rate, using the SM+CVC rate, or ignored completely. The onset of each electron capture is labeled with the parent nucleus. Note that for simulations including the forbidden transition capture on  $^{24}\text{Na}$  does not occur separately from capture on  $^{24}\text{Mg}$ .

resulting rate is comparatively slow the heating from the  $^{20}\text{Ne}(e^-, \nu_e)^{20}\text{F}(e^-, \nu_e)^{20}\text{O}$  double electron capture is gradual and it is temporarily canceled by the cooling from the  $^{25}\text{Na} \leftrightarrow ^{25}\text{Ne}$  Urca process. After the exhaustion of  $^{25}\text{Na}$  in the center the heating resumes and eventually ignites runaway oxygen burning: Our simulations stop when the energy from the oxygen burning exceeds the thermal neutrino losses. Prior to this a substantial fraction of the central  $^{20}\text{Ne}$  has been converted into  $^{20}\text{O}$ . If the depletion is large enough ignition occurs mildly off-center where there is more  $^{20}\text{Ne}$  left.

TABLE VII. Ignition densities and radii with and without the forbidden transition between  $^{24}\text{Na}$  and  $^{24}\text{Ne}$  (assuming the SM+CVC rate).

$\dot{M}$ ( $M_\odot \text{ yr}^{-1}$ )	$\rho_c^{\text{ign}}$ ( $\text{g cm}^{-3}$ )		$R_{\text{ign}}$ (km)	
	Without	With	Without	With
$10^{-7}$	9.43	9.52	58	62
$10^{-6}$	9.13	9.21	35	42
$10^{-5}$	8.64	8.64	< 10	< 10

In the final phase the simulations with and without the forbidden transition between  $^{24}\text{Na}$  and  $^{24}\text{Ne}$  again diverge, although only slightly. We summarize the effects on the ignition density and radii for the three different growth rates in Table VII. The only discernible change occurs in the simulations with off-center ignition: in these cases the ignition density is slightly reduced while the ignition radius grows by 4–7 km.

To also illustrate the off-center differences between the models Fig. 6 presents the temperature profiles at the end

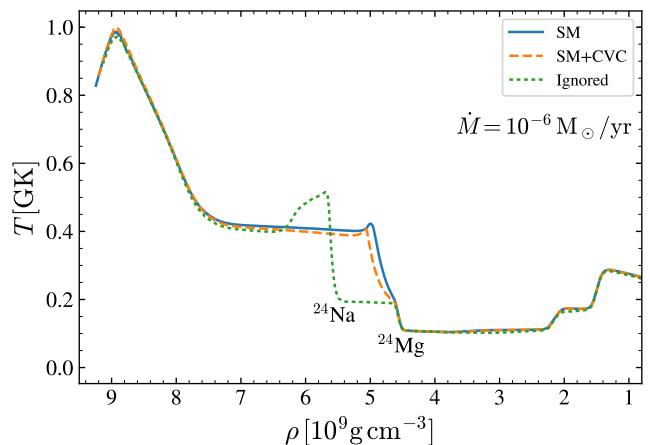


FIG. 6. Temperature profiles at ignition for the models in Fig. 5. Note that we plot the temperature as a function of density as opposed to radius. We label the approximate locations where electron capture on  $^{24}\text{Mg}$  and (when occurring separately)  $^{24}\text{Na}$  is taking place.

of the simulations. The spatial variation in temperature partially mirrors the temporal evolution in Fig. 5. Note that electron capture processes that have ceased in the center are still taking place further out where the density is lower. We have marked the approximate locations of electron capture on  $^{24}\text{Mg}$  and  $^{24}\text{Na}$ . As before the inclusion of the forbidden transition means that the reactions occur in close succession, whereas without this transition the increase in temperature occurs in two separate steps. Further towards the center the differences between the models are minimal.

The above results would suggest that the forbidden transition only has a minor impact on the ignition conditions. However, as described in Ref. [15] the steep temperature gradient arising from electron capture on  $^{24}\text{Mg}$  and  $^{24}\text{Na}$  induces convective instabilities that cannot be modeled in the present version of MESA. Further work is needed to determine their implications. As the forbidden transition affects the appearance of the temperature gradients it should be included in future work.

The evolution of the core is of course sensitive to the details of the composition, which is determined by the preceding carbon burning. A special case arises when there is a substantial amount of residual  $^{12}\text{C}$  in the core. This has recently been investigated in Ref. [48]. Following the same procedure, we have run MESA simulations presented in Fig. 7. The composition is taken as  $X(^{12}\text{C}) = 0.01$  and  $X(^{20}\text{Ne}) = 0.38$  with other mass fractions remaining the same as before. In all three cases, the electron captures ignite runaway carbon burning, but when the forbidden transition is included this occurs at significantly lower densities than before. The difference between using the SM and SM+CVC rates is as before negligible. Due to numerical difficulties resulting from convection triggered by the carbon burning (see Ref. [48])

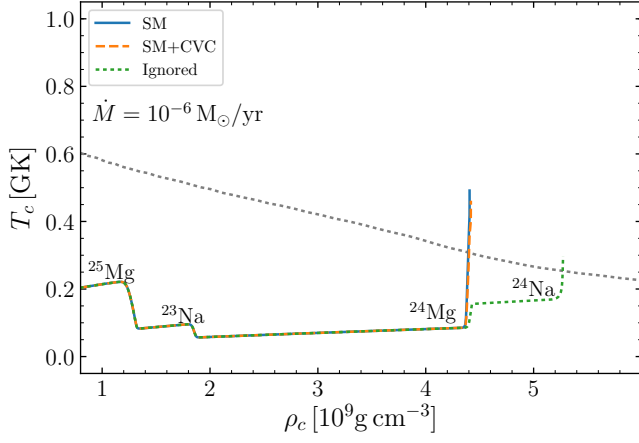


FIG. 7. Evolution of central temperature and density as in Fig. 5, but with the core having a residual carbon mass fraction of  $X(^{12}\text{C}) = 0.01$ . The dotted gray line is the carbon ignition curve taken from Fig. 6 in Ref. [48]. Along this curve energy generation from carbon burning equals thermal neutrino losses.

for details) we are unable to follow the subsequent evolution of the core towards oxygen ignition. Nevertheless, the above results indicate that the forbidden transition is of significance for cores with residual carbon.

### B. $^{27}\text{Al} \leftrightarrow ^{27}\text{Mg}$

An Urca process affects the temperature if it has enough time to release a significant amount of neutrinos before it ceases to operate. In quantitative terms, the cooling timescale  $t_{\text{cool}}$  must be shorter than the timescale  $t_{\text{cross}}$  it takes to cross the density range where the Urca process is active. Ref. [15] derives the following approximations

$$t_{\text{cool}} \approx 4 \times 10^2 \left( \frac{T}{10^8 \text{ K}} \right)^{-3} \left( \frac{X}{0.01} \right)^{-1} \times \left( \frac{Q}{5 \text{ MeV}} \right)^{-2} \left( \frac{ft}{10^5 \text{ s}} \right) \text{ yrs} \quad (18)$$

$$t_{\text{cross}} \approx 2 \times 10^{-2} \left( \frac{T}{10^8 \text{ K}} \right) \left( \frac{\rho}{10^9 \text{ g cm}^{-3}} \right)^{-1/3} t_{\rho}. \quad (19)$$

Here  $X$  is the initial mass fraction of the parent nucleus,  $Q$  is the energy difference between the initial and final states, and  $ft$  describes the strength of the transition. Furthermore,  $t_{\rho} = (d \ln \rho_c / dt)^{-1}$  is the compression timescale that sets the pace of the density growth. From Ref. [14] we have the expression

$$t_{\rho} \approx 5 \times 10^4 \left( \frac{\rho}{10^9 \text{ g cm}^{-3}} \right)^{-0.55} \times \left( \frac{\dot{M}}{10^{-6} \text{ M}_{\odot} \text{ yr}^{-1}} \right)^{-1} \text{ yr} \quad (20)$$

which was derived by modeling the core as a zero-temperature white dwarf in hydrostatic equilibrium with  $Y_e \approx 0.5$  and  $\rho \sim 10^9 - 10^{10} \text{ g cm}^{-3}$ . While the threshold density for capture on  $^{27}\text{Al}$  is somewhat lower than this ( $\rho \approx 5 \times 10^8 \text{ g cm}^{-3}$ ) the approximation in (20) is still acceptable for our purposes.

For the forbidden transition, we have  $Q \approx 3 \text{ MeV}$  and  $\log ft \approx 11$ . Furthermore, simulations [2, 3] of the carbon burning stage indicate that  $X < 0.01$ . Given a slow growth rate of  $\dot{M} = 10^{-7} \text{ M}_{\odot} \text{ yr}^{-1}$  we then have that  $t_{\text{cool}} < t_{\text{cross}}$  at the threshold density only if  $T \gtrsim 1.6 \text{ GK}$ . For larger values of  $\dot{M}$  the required temperature is even higher. As we expect that  $T \lesssim 1 \text{ GK}$  prior to oxygen ignition we can conclude that the Urca cooling due to the forbidden transition is negligible. At such high temperatures the electron capture and  $\beta^-$  decay rates would in any case be dominated by allowed transitions.

Despite the weakness of the forbidden transition the timescale  $(\lambda_{\text{forbidden}}^{\text{EC}})^{-1}$  of the corresponding electron capture rate will still fall below the compression timescale  $t_{\rho}$ . This means that the onset of  $^{27}\text{Al}(e^-, \nu_e)^{27}\text{Mg}$  is not delayed until the threshold density for the allowed  $5/2_{\text{g.s.}}^+ \rightarrow 3/2_1^+$  transition is reached. As a consequence the mild heating due to the gamma decay of the  $3/2^+$  state, as seen in Fig. 8 of Ref. [48], would likely not occur. This effect is at any rate small and occurs comparatively early in the evolution of the core. It is thus reasonable to conclude that the forbidden transition does not have any significant impact on the ignition conditions.

## VI. CONCLUSIONS

We have provided a more detailed account of the formalism used in Ref. [19, 20]. Furthermore, we have investigated two additional second-forbidden non-unique transitions ( $\Delta J^{\pi} = 2^+$ ) of relevance to degenerate ONe cores: the  $4_{\text{g.s.}}^+ \rightarrow 2_1^+$  transition from  $^{24}\text{Na}$  to  $^{24}\text{Ne}$ , and the  $5/2_{\text{g.s.}}^+ \rightarrow 1/2_{\text{g.s.}}^+$  transition from  $^{27}\text{Al}$  to  $^{27}\text{Mg}$ . The necessary nuclear matrix elements have been determined through shell-model calculations (SM) in combination with constraints from CVC theory (SM+CVC). We have calculated the axial matrix elements using both bare ( $g_A = -1.276$ ) and quenched ( $g_A = -1.0$ ) values of the axial coupling constant. To test our approach we have applied it to the previously measured  $4_{\text{g.s.}}^+ \rightarrow 2_1^+$  transition in the  $\beta^-$  decay of  $^{24}\text{Na}$ .

For the decay of  $^{24}\text{Na}$  our calculated rate is within a factor 1 to 3 of the value given by Ref. [42]. However, when extrapolating from the measured region of the electron energy spectrum the authors of Ref. [42] had assumed an allowed spectrum shape: in reality the difference between the theoretical and measured rates may be as high as a factor 3 to 6. We arrived at the best agreement by using the SM+CVC approach, with quenching applied to the axial nuclear matrix elements.

The forbidden transition between  $^{24}\text{Na}$  and  $^{24}\text{Ne}$  has a substantial impact on the electron capture rate for tem-

peratures  $\log_{10}(T[\text{K}]) \lesssim 8.5$ . It lowers the threshold density for  $^{24}\text{Na}(e^-, \nu_e)^{24}\text{Ne}$  so that it can occur immediately following the onset of  $^{24}\text{Mg}(e^-, \nu_e)^{24}\text{Na}$ . To illustrate the astrophysical impact we performed simulations using the stellar evolution code MESA according to the procedures detailed in Ref. [14, 15, 48]. The effects do not appear to be very sensitive to uncertainties in the rate: the SM and SM+CVC rates produce very similar results despite being up to a factor 3 different. In general the impact on the ignition conditions appears negligible, but there is a change in the radial temperature gradients arising from the  $A = 24$  captures. These gradients are known to cause convectional instabilities that are not accounted for in our simulations and future work should include the forbidden transition. Finally, we note that in models where burning of residual  $^{12}\text{C}$  occurs the forbidden transition reduces the carbon ignition density.

The forbidden transition between the ground states of  $^{27}\text{Al}$  to  $^{27}\text{Mg}$  permits the onset of electron capture at lower densities, precluding the minor heating associated with capture into excited states. However, the transition strength is too small to produce any significant cooling during the time that the stellar core spends in the density range where Urca cycles occur. Considering the early onset and small impact of this electron capture reaction, we expect its significance for the ignition conditions to be minimal. However, we still recommend that this transition is included when calculating the electron capture and  $\beta^-$  decay rates between  $^{27}\text{Al}$  and  $^{27}\text{Mg}$  for conditions  $\log_{10}(T[\text{K}]) \lesssim 8.8$ .

## ACKNOWLEDGMENTS

The authors thank Oliver S. Kirsebom for his comments on the manuscript. DFS and GMP acknowl-

edge the support of the Deutsche Forschungsgemeinschaft (DFG, German Research Foundation) – Project-ID 279384907 – SFB 1245 “Nuclei: From Fundamental Interactions to Structure and Stars”, the Helmholtz Forschungsakademie Hessen für FAIR, and the ChETEC COST action (CA16117), funded by COST (European Cooperation in Science and Technology).

## Appendix A: Shape factors

For second-forbidden non-unique transitions the shape factor can be written (see Ref. [24]) as the sum

$$C(w) = \sum_{k_e+k_\nu=3} \lambda_{k_e} \left\{ M_2^2(k_e, k_\nu) + m_2^2(k_e, k_\nu) - \frac{2\mu_{k_e}\gamma_{k_e}}{k_e w} M_2(k_e, k_\nu) m_2(k_e, k_\nu) \right\} \quad (\text{A1})$$

$$+ \sum_{k_e+k_\nu=4} \lambda_{k_e} \{ \tilde{M}_2^2(k_e, k_\nu) + \tilde{M}_3^2(k_e, k_\nu) \}$$

where the indices  $k_e$  and  $k_\nu$  run over the positive integers. Furthermore, we have  $\gamma_k = \sqrt{k^2 - (\alpha Z)^2}$  and assume  $\lambda_{k_e} \approx 1$  and  $\mu_{k_e} \approx 1$ . The two latter quantities arise due to the Coulomb interaction between the nucleus and the electron and the approximations are valid for the small  $Z$  we encounter in this work.  $M_K(k_e, k_\nu)$  and  $m_K(k_e, k_\nu)$  contain the form factor coefficients and are given by

$$M_2(k_e, k_\nu) = \frac{2(p_e R)^{k_e-1} (p_\nu R)^{k_\nu-1}}{\sqrt{15}(2k_e-1)!(2k_\nu-1)!} \left\{ -\sqrt{\frac{5}{2}} V_{F_{211}}^{(0)} \mp \frac{\alpha Z}{2k_e+1} V_{F_{220}}^{(0)}(k_e, 1, 1, 1) \right. \quad (\text{A2})$$

$$\left. \mp \left[ \frac{wR}{2k_e+1} \pm \frac{p_\nu R}{2k_\nu+1} \right] V_{F_{220}}^{(0)} - \frac{\alpha Z}{2k_e+1} \sqrt{\frac{3}{2}} {}^A F_{221}^{(0)}(k_e, 1, 1, 1) - \left[ \frac{wR}{2k_e+1} \mp \frac{p_\nu R}{2k_\nu+1} \right] \sqrt{\frac{3}{2}} {}^A F_{221}^{(0)} \right\}$$

$$m_2(k_e, k_\nu) = \mp \frac{2(p_e R)^{k_e-1} (p_\nu R)^{k_\nu-1}}{\sqrt{15}(2k_e-1)!(2k_\nu-1)!} \frac{R}{2k_e+1} \left\{ V_{F_{220}}^{(0)} \pm \sqrt{\frac{3}{2}} {}^A F_{221}^{(0)} \right\} \quad (\text{A3})$$

$$\tilde{M}_2(k_e, k_\nu) = \pm 2 \frac{\sqrt{2}(p_e R)^{k_e-1} (p_\nu R)^{k_\nu-1}}{\sqrt{5}(2k_e-1)(2k_\nu-1)(2k_e-1)!(2k_\nu-1)!} \left\{ V_{F_{220}}^{(0)} \mp \frac{k_e - k_\nu}{3} \sqrt{\frac{3}{2}} {}^A F_{221}^{(0)} \right\} \quad (\text{A4})$$

$$\tilde{M}_3(k_e, k_\nu) = -2 \frac{2(p_e R)^{k_e-1} (p_\nu R)^{k_\nu-1}}{\sqrt{15}(2k_e-1)!(2k_\nu-1)!} {}^A F_{321}^{(0)}. \quad (\text{A5})$$

In these expressions  $p_e$  and  $p_\nu$  are the electron and neutrino momenta in units of  $m_e c$  and  $R$  refers to the nuclear

radius in units of the reduced electron Compton wavelength  $\lambda_e = \hbar/(m_e c)$ . Upper signs apply to  $\beta^-$  decay

while lower signs correspond to electron capture. Note that the latter case was derived in Ref. [24, 25] assuming orbital electron capture. We can with some modifications apply this derivation to continuum electron capture as shown in Ref. [26].

One can compare the shape factor for  $\beta^-$  decay from an initial state  $i$  to a final state  $f$  with the shape factor of the reverse electron capture from  $f$  to  $i$ . For a given electron energy  $w$  the neutrino momentum has opposite signs in the two cases:

$$p_\nu^{\beta^-} = q_{if}^{\beta^-} - w = -(q_{fi}^{\text{EC}} + w) = -p_\nu^{\text{EC}}. \quad (\text{A6})$$

Furthermore, the form factor coefficients follow the relation

$$\begin{aligned} \left[ V/A F_{KLS}^{(N)} \right]_{f \rightarrow i}^{\text{EC}} &= (-1)^{K-s+J_i-J_f} \\ &\times \frac{\sqrt{2J_i+1}}{\sqrt{2J_f+1}} \left[ V/A F_{KLS}^{(N)} \right]_{i \rightarrow f}^{\beta^-} \end{aligned} \quad (\text{A7})$$

which of course also applies to coefficients of the type  $V/A F_{KLS}^{(N)}(k_e, m, n, \rho)$ . Note that Ref. [24, 25] arrived at a similar equation when exchanging initial and final states in the reduced lepton matrix elements. As shown in Ref. [49] the sign change in (A7) ultimately arises from the conjugation properties of the corresponding spherical tensor operators.

If we insert (A7) and (A6) into (A1)–(A5) we arrive at

$$C_{f \rightarrow i}^{\text{EC}}(w) = \frac{2J_i+1}{2J_f+1} C_{i \rightarrow f}^{\beta^-}(w). \quad (\text{A8})$$

In other words the shape factors for  $\beta^-$  decay and for the reverse electron capture are given by the same expression, up to a trivial factor correcting for the exchange of the initial and final angular momenta. The key difference instead lies in the domain of the two shape factors: for  $\beta^-$  decay the electron energy cannot exceed the decay  $Q$  value ( $w < q_{if}$ ) whereas for electron capture the energy must instead be larger than this value ( $w > q_{if}$ , assuming  $q_{if} > 1$ ). One can view  $C^{\text{EC}}(w)$  as an extension of  $C^{\beta^-}(w)$  to higher energies.

One should note that (A8) does not apply when comparing stellar electron capture to  $\beta^-$  decay measured in the laboratory. This is due to the Coulomb correction (8a) which means that  $q_{if}^{\text{EC,med}} \neq -q_{fi}^{\beta^-}$ , thus invalidating (A6). The relationship used in Ref. [19] between the forbidden  $^{20}\text{Ne} \rightarrow ^{20}\text{F}$  electron capture to the measured  $\beta^-$  decay of  $^{20}\text{F}$  corrected for this fact by first computing the electron capture shape factor for arbitrary  $q_{if}^{\text{EC,med}}$  and then rescaling it by the same amount as the fitted  $\beta^-$  decay shape factor so that (A8) was recovered in the limit of no Coulomb correction.

## Appendix B: $I(k_e, m, n, \rho)$ factors

In addition to the regular matrix elements  $V/A \mathfrak{M}_{KLS}^{(N)}$ , we also need to calculate  $V/A \mathfrak{M}_{KLS}^{(N)}(k_e, m, n, \rho)$  where the operator is multiplied by a factor  $I(k_e, m, n, \rho; r)$ . Although this factor depends on how the nuclear charge distribution is parameterized, it has been shown [23] that it is not very sensitive to the precise form. For simplicity, we can then assume a spherical uniform distribution for which the factors we need in this work can be written

$$I(k_e, 1, 1, 1; r) = \begin{cases} \frac{3}{2} - \frac{2k_e+1}{2(2k_e+3)} \left( \frac{r}{R} \right)^2, & 0 \leq r \leq R \\ \frac{2k_e+1}{2k_e} \frac{R}{r} - \frac{3}{2k_e(2k_e+3)} \left( \frac{R}{r} \right)^{2k_e+1}, & r \geq R. \end{cases} \quad (\text{B1})$$

Furthermore, one can show that we have the general property  $I(k_e, m, n, 0) = 1$ . This means that we can put matrix elements with and without these factors on an equal footing by writing

$$V/A \mathfrak{M}_{KLS}^{(N)} = V/A \mathfrak{M}_{KLS}^{(N)}(k_e, m, n, 0).$$

## Appendix C: Single-particle matrix elements

The nuclear matrix elements can be decomposed as

$$\begin{aligned} V/A \mathfrak{M}_{KLS}^{(N)}(k_e, n, n, \rho) &= \\ \frac{1}{\sqrt{2J_i+1}} \sum_{\alpha\beta} \frac{\langle \psi_f || [a_\alpha^\dagger \otimes \tilde{a}_\beta]^K || \psi_i \rangle}{\sqrt{2K+1}} & \quad (\text{C1}) \\ \times V/A m_{KLS}^{(N)}(k_e, m, n, \rho)(\alpha\beta) \end{aligned}$$

where  $\psi_i$  and  $\psi_f$  are the initial and final nuclear states and the summation indices  $\alpha$  and  $\beta$  run over all single-nucleon states in the valence space. Here  $\langle \psi_f || [a_\alpha^\dagger \otimes \tilde{a}_\beta]^K || \psi_i \rangle$  is the reduced one-body transition density (which we get from our shell model calculations) and  $V/A m_{KLS}^{(0)}(k_e, m, n, \rho)(\alpha\beta)$  is the associated single-particle matrix element. Note that for  $\beta^-$  decay  $\alpha$  denotes a proton and  $\beta$  denotes a neutron, with the opposite being the case for electron capture.

A derivation of the single-particle matrix elements can be found in Ref. [24]. It should be noted that the authors follow the Biedenharn-Rose (BR) phase convention [50] while our shell model calculations use the Condon-Shortley (CS) convention [51]. This means that expressions for the single-particle matrix elements must be modified so that they can be used with one-body transition densities in the CS convention.

The formalism in Ref. [24] is fully relativistic and the single-nucleon states are thus given by spinors. If we follow the CS convention but otherwise adhere to the

definitions given in Ref. [24] we can write these states as

$$\phi_{\kappa\mu}(\mathbf{r}) = \begin{pmatrix} -if_{\kappa}(r)\chi_{-\kappa\mu} \\ g_{\kappa}(r)\chi_{\kappa\mu} \end{pmatrix} \quad (\text{C2})$$

where the quantum number  $\kappa$  determines both  $l$  and  $j$  and is defined by

$$\kappa = \begin{cases} j + \frac{1}{2} & \text{for } l = j + \frac{1}{2} \\ -(j + \frac{1}{2}) & \text{for } l = j - \frac{1}{2} \end{cases}$$

and where  $\chi_{\kappa\mu}$  is the spin-angular part

$$\chi_{\kappa\mu} = [Y_l(\hat{r}) \otimes \chi_{1/2}]_{\kappa\mu}. \quad (\text{C3})$$

The functions  $g_{\kappa}(r)$  and  $f_{\kappa}(r)$  are solutions to the radial Dirac equation. As described in Ref. [24] we can relate these functions to non-relativistic nuclear models (such as the shell model) by taking the non-relativistic limit of the radial equations.  $g_{\kappa}(r)$  then becomes the solution of the corresponding radial Schrödinger equation whereas  $f_{\kappa}(r)$  is given by

$$f_{\kappa}(r) = \frac{1}{2M_N} \left( \frac{d}{dr} + \frac{\kappa + 1}{r} \right) g_{\kappa}(r) \quad (\text{C4})$$

with  $M_N$  being the nucleon mass in units of  $m_e$ . For the

harmonic oscillator basis we use in this work we have

$$g_{n\kappa}(r) = \sqrt{\frac{2n!}{b^3(n+l+1/2)!}} \left( \frac{r}{b} \right)^l \times \exp(-r^2/2b^2) L_n^{l+\frac{1}{2}}(r^2/b^2) \quad (\text{C5})$$

$$f_{n\kappa}(r) = \frac{1}{2M_N} \left[ \left( \frac{1+\kappa+l}{r} + \frac{r}{b^2} \right) g_{nl}(r) - \frac{2}{b} \sqrt{n+l+\frac{3}{2}} g_{nl+1}(r) \right] \quad (\text{C6})$$

where  $L_n^{l+\frac{1}{2}}(x)$  is the associated Laguerre polynomial and  $b$  is the oscillator length. Note that  $r$  and  $b$  are like the nuclear radius  $R$  given in units of the reduced electron Compton wavelength  $\lambda_e = \hbar/(m_e c)$ .

To arrive at the single-particle matrix elements in the CS convention we replace the BR single-particle states in Ref. [24] with our new CS states given by (C2). We then have to factor out a global complex phase factor to keep our single-particle matrix elements real. We describe this in more detail in Ref. [26]. The final expressions are as follows:

$$V m_{KK0}^{(N)}(k_e, m, n, \rho)(\alpha\beta) = \sqrt{2} \left\{ G_{KK0}(\kappa_{\alpha}, \kappa_{\beta}) \int_0^{\infty} g_{n_{\alpha}, \kappa_{\alpha}}(r) \left( \frac{r}{R} \right)^{K+2N} I(k_e, m, n, \rho; r) g_{n_{\beta}, \kappa_{\beta}}(r) r^2 dr \right. \\ \left. + G_{KK0}(-\kappa_{\alpha}, -\kappa_{\beta}) \int_0^{\infty} f_{n_{\alpha}, \kappa_{\alpha}}(r) \left( \frac{r}{R} \right)^{K+2N} I(k_e, m, n, \rho; r) f_{n_{\beta}, \kappa_{\beta}}(r) r^2 dr \right\} \quad (\text{C7a})$$

$$A m_{KL1}^{(N)}(k_e, m, n, \rho)(\alpha\beta) = \text{sgn}(K - L + 1/2) \\ \times \sqrt{2} \left\{ G_{KL1}(\kappa_{\alpha}, \kappa_{\beta}) \int_0^{\infty} g_{n_{\alpha}, \kappa_{\alpha}}(r) \left( \frac{r}{R} \right)^{L+2N} I(k_e, m, n, \rho; r) g_{n_{\beta}, \kappa_{\beta}}(r) r^2 dr \right. \\ \left. + G_{KL1}(-\kappa_{\alpha}, -\kappa_{\beta}) \int_0^{\infty} f_{n_{\alpha}, \kappa_{\alpha}}(r) \left( \frac{r}{R} \right)^{L+2N} I(k_e, m, n, \rho; r) f_{n_{\beta}, \kappa_{\beta}}(r) r^2 dr \right\} \quad (\text{C7b})$$

$$A m_{KK0}^{(N)}(k_e, m, n, \rho)(\alpha\beta) = \sqrt{2} \left\{ G_{KK0}(\kappa_{\alpha}, -\kappa_{\beta}) \int_0^{\infty} g_{n_{\alpha}, \kappa_{\alpha}}(r) \left( \frac{r}{R} \right)^{K+2N} I(k_e, m, n, \rho; r) f_{n_{\beta}, \kappa_{\beta}}(r) r^2 dr \right. \\ \left. - G_{KK0}(-\kappa_{\alpha}, \kappa_{\beta}) \int_0^{\infty} f_{n_{\alpha}, \kappa_{\alpha}}(r) \left( \frac{r}{R} \right)^{K+2N} I(k_e, m, n, \rho; r) g_{n_{\beta}, \kappa_{\beta}}(r) r^2 dr \right\} \quad (\text{C7c})$$

$$V m_{KL1}^{(N)}(k_e, m, n, \rho)(\alpha\beta) = \text{sgn}(L - K + 1/2) \\ \times \sqrt{2} \left\{ G_{KL1}(\kappa_{\alpha}, -\kappa_{\beta}) \int_0^{\infty} g_{n_{\alpha}, \kappa_{\alpha}}(r) \left( \frac{r}{R} \right)^{L+2N} I(k_e, m, n, \rho; r) f_{n_{\beta}, \kappa_{\beta}}(r) r^2 dr \right. \\ \left. - G_{KL1}(-\kappa_{\alpha}, \kappa_{\beta}) \int_0^{\infty} f_{n_{\alpha}, \kappa_{\alpha}}(r) \left( \frac{r}{R} \right)^{L+2N} I(k_e, m, n, \rho; r) g_{n_{\beta}, \kappa_{\beta}}(r) r^2 dr \right\}. \quad (\text{C7d})$$

Our expressions contain the quantity  $G_{KLs}(\kappa_1, \kappa_2)$  which

holds the spin-angular matrix element. In the CS con-

vention it is given by the expression

$$G_{KLS}(\kappa_1, \kappa_2) = (-1)^{j_2-j_1+l_1} \sqrt{(2s+1)(2K+1)} \\ \times \sqrt{(2j_1+1)(2j_2+1)} \sqrt{(2l_1+1)(2l_2+1)} \\ \times \left\langle l_1 l_2 00 \middle| L0 \right\rangle \begin{Bmatrix} K & s & L \\ j_1 & \frac{1}{2} & l_1 \\ j_2 & \frac{1}{2} & l_2 \end{Bmatrix}.$$

#### Appendix D: Population of isomeric state in $^{24}\text{Na}$

Ref. [14] argues that the population of the isomeric state in  $^{24}\text{Na}$  would follow a thermal distribution since the gamma decay rate, while slow, would still be substantially faster the electron capture rate. Here, we reexamine this issue by describing the population of the different states as the steady-state solution to a set of differential equations following the approach of Ref. [52].

Note that we only need to consider the first three states ( $4_{\text{g.s.}}^+$ ,  $1_1^+$  and  $2_1^+$ ) since all others have excitation energies well above 1 MeV. We denote the number density of  $^{24}\text{Na}$  nuclei in the  $4_{\text{g.s.}}^+$  state by  $n_1$  and let  $n_2$  and  $n_3$  be the corresponding quantities for the  $1_1^+$  and  $2_1^+$  states. Given this we can write

$$\frac{dn_1}{dt} = -(\lambda_{12}^\gamma + \lambda_{13}^\gamma + \lambda_{1d}^{\text{EC}})n_1 + \lambda_{21}^\gamma n_2 + \lambda_{31}^\gamma n_3 \quad (\text{D1})$$

$$\frac{dn_2}{dt} = \lambda_{12}^\gamma n_1 - (\lambda_{21}^\gamma + \lambda_{23}^\gamma + \lambda_{2d}^{\text{EC}})n_2 + \lambda_{32}^\gamma n_3 \\ + \lambda_{p2}^{\text{EC}} n_p \quad (\text{D2})$$

$$\frac{dn_3}{dt} = \lambda_{13}^\gamma n_1 + \lambda_{23}^\gamma n_2 - (\lambda_{31}^\gamma + \lambda_{32}^\gamma)n_3. \quad (\text{D3})$$

Here  $\lambda_{id}^{\text{EC}}$  is the sum of all partial electron capture rates from a state  $i$  to any state in the daughter nucleus  $^{24}\text{Ne}$ . Furthermore,  $n_p$  is the number density of the parent nucleus  $^{24}\text{Mg}$  and  $\lambda_{pi}^{\text{EC}}$  is the total electron capture rate from  $^{24}\text{Mg}$  to a state  $i$  in  $^{24}\text{Na}$ . Note that in (D1)–(D3) we only include the electron capture transitions shown in Fig. 1. Finally,  $\lambda_{ij}^\gamma$  refers to the gamma decay or excitation rate from a state  $i$  to a state  $j$ . We get the decay rates  $\lambda_{21}^\gamma = 3.43 \times 10^1 \text{ s}^{-1}$ ,  $\lambda_{31}^\gamma = 6.78 \times 10^8 \text{ s}^{-1}$  and  $\lambda_{32}^\gamma = 1.86 \times 10^{10} \text{ s}^{-1}$  from Ref. [41] and the inverse excitation rates via detailed balance as

$$\lambda_{ji}^\gamma = \frac{2J_i + 1}{2J_j + 1} \exp\left(-\frac{E_i - E_j}{kT}\right) \lambda_{ij}^\gamma. \quad (\text{D4})$$

The solution to (D1)–(D3) is in general time-dependent, but will approach a steady-state solution as time goes by. In this limit the ratio between the probabilities of occupying the  $1_1^+$  and  $4_{\text{g.s.}}^+$  states is given by

$$\frac{P_2}{P_1} = \frac{n_2}{n_1} = \frac{(\lambda_{12}^\gamma + \lambda_{13}^\gamma + \lambda_{1d}^{\text{EC}})(\lambda_{31}^\gamma + \lambda_{32}^\gamma) - \lambda_{13}^\gamma \lambda_{31}^\gamma}{\lambda_{21}^\gamma (\lambda_{31}^\gamma + \lambda_{32}^\gamma) + \lambda_{23}^\gamma \lambda_{31}^\gamma}. \quad (\text{D5})$$

Note that if the electron captures are much slower than the internal transitions we have

$$\lambda_{1d}^{\text{EC}} \ll \lambda_{12}^\gamma + \lambda_{13}^\gamma \quad (\text{D6})$$

in which case (D5) can be shown to equal the thermal-equilibrium ratio

$$\frac{P_2}{P_1} = \frac{2J_2 + 1}{2J_1 + 1} \exp\left(-\frac{E_2}{kT}\right). \quad (\text{D7})$$

This corresponds to the Boltzmann distribution assumed in (1) and (12).

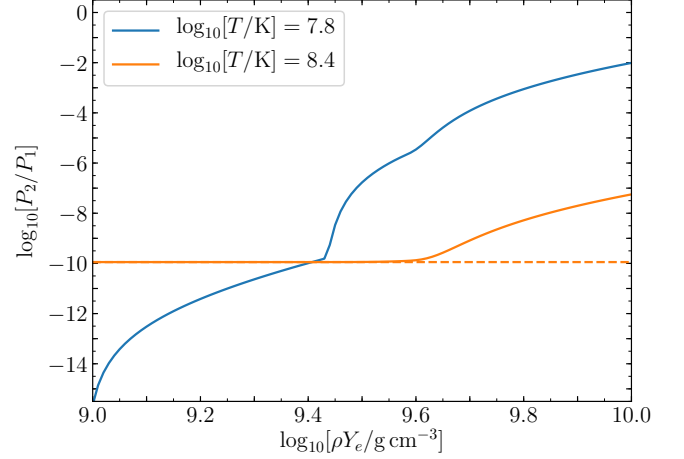


FIG. 8. Ratio between the probabilities of occupying the  $1_1^+$  and  $4_{\text{g.s.}}^+$  states as a function of the density. Solid lines corresponds to the steady-state expression (D5) and dashed lines to the thermal-equilibrium limit (D7). Note that there is no dashed blue line as (D7) is negligible ( $\log_{10}(P_2/P_1) < -38$ ) for  $\log_{10}(T[\text{K}]) = 7.8$ .

We plot (D5) and (D7) as a function of the density in Fig. 8. For  $\log_{10}(T[\text{K}]) = 8.4$  the two coincide as long as  $\log_{10}(\rho Y_e [\text{g cm}^{-3}]) \lesssim 9.5$ . At higher densities  $\lambda_{1d}^{\text{EC}}$  is so large that (D6) no longer applies. As a consequence the thermal-equilibrium limit now underestimates the population of the  $1_1^+$  state. However, in our MESA simulations  $^{24}\text{Na}$  has already been depleted when this density is reached. This means that it is still appropriate to describe the population of the excited states using a Boltzmann distribution at this temperature. The situation is quite different for  $\log_{10}(T[\text{K}]) = 7.8$ . At such low temperatures  $\lambda_{12}^\gamma$  and  $\lambda_{13}^\gamma$  are so small that (D6) is violated for all relevant densities, meaning that we cannot expect the thermal-equilibrium limit to be a good approximation to the steady-state solution at all. Indeed, (D7) underestimates the  $P_2/P_1$  ratio by tens of orders of magnitude compared to (D5). Note that for  $\log_{10}(\rho Y_e [\text{g cm}^{-3}]) \gtrsim 9.4$  the population of the  $1_1^+$  state is lower at  $\log_{10}(T[\text{K}]) = 8.4$  than at  $\log_{10}(T[\text{K}]) = 7.8$ . This is because higher temperatures favors excitation from the  $1_1^+$  state to the  $2_1^+$  state. The latter is not an isomer and quickly decays to the ground state.

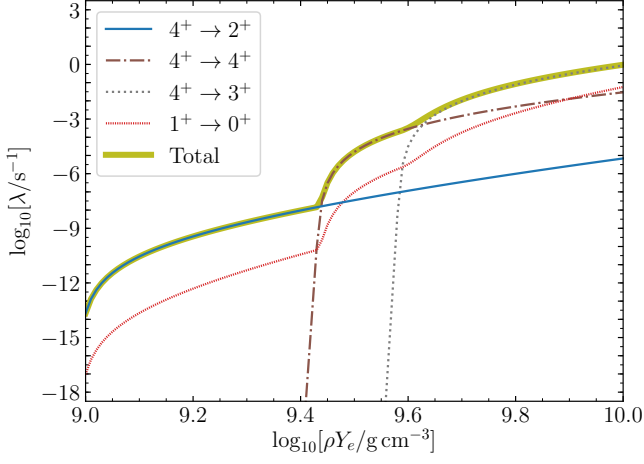


FIG. 9. Electron capture rates on  $^{24}\text{Na}$  at  $\log_{10}(T[\text{K}]) = 7.8$  assuming that the relative population of the  $1_1^+$  state is given by (D5).

In Fig. 9 we illustrate the impact of the non-thermal population at  $\log_{10}(T[\text{K}]) = 7.8$  on the  $^{24}\text{Na}(e^-, \nu_e)^{24}\text{Ne}$  rate. Note that while the population of the  $1_1^+$  state is dramatically higher relative to the thermal equilibrium the probability of a nucleus occupying the  $4_{\text{g.s.}}^+$  ground state is still very close to 1. Consequently the electron capture rate via the  $4_{\text{g.s.}}^+ \rightarrow 2_1^+$ ,  $4_{\text{g.s.}}^+ \rightarrow 3_1^+$  and  $4_{\text{g.s.}}^+ \rightarrow 4_1^+$  transitions are practically the same as when assuming thermal equilibrium (i.e. as in the lower panel of Fig. 2). In contrast, the contribution from the  $1_1^+ \rightarrow 0_{\text{g.s.}}^+$  transition is now much larger than before. However, it is still dwarfed by the rate of electron capture on the ground state and the total rate is virtually unaffected. This would also be true even if we ignored the forbidden transition:  $\lambda_{1d}^{\text{EC}}$  would then be essentially zero for  $\log_{10}(\rho Y_e [\text{g cm}^{-3}]) \lesssim 9.4$  and (D6) would still apply in this range. Given the above we conclude that assuming thermal equilibrium will still give us the correct total electron capture rate.

The reader may ask whether the non-thermal population could affect the neutrino loss rate (12). We have computed this quantity at  $\log_{10}(T[\text{K}]) = 7.8$  as shown in Fig. 10. In this case the enhancement of the contribution from the  $1_1^+ \rightarrow 0_{\text{g.s.}}^+$  transition appears to be larger than in Fig. 9. However, the neutrino loss rate is still dominated by transitions from the ground state, which are not affected by the higher relative population of the  $1_1^+$  state. In conclusion, a thermal distribution also appears to yield the correct neutrino loss rate.

#### Appendix E: Calculation of the forbidden electron capture rate in MESA

For allowed transitions MESA is able to calculate  $\beta^-$  decay and electron capture rates directly. This capability was introduced in Ref. [14, 53] and allows to avoid the in-

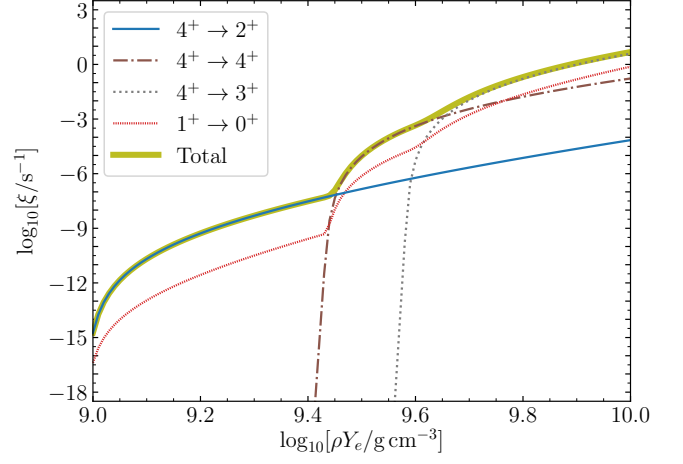


FIG. 10. Neutrino loss rates for the electron capture on  $^{24}\text{Na}$  at  $\log_{10}(T[\text{K}]) = 7.8$ , assuming that the relative population of the  $1_1^+$  state is given by (D5).

terpolating errors associated with using tabulated rates. In practice, the implementation is based on rewriting the rate expressions in terms of Fermi integrals

$$F_k(\eta) = \int_0^\infty \frac{x^k}{\exp(x - \eta) + 1} dx \quad (\text{E1})$$

as MESA already includes efficient routines to evaluate such quantities. We wish to do the same for the electron capture via second-forbidden transitions and we will now provide the corresponding expressions.

As in Ref. [14] we start by writing

$$\frac{p_e}{w} F(Z, w) \approx \exp(\pi \alpha Z) \quad (\text{E2})$$

which is a valid approximation for light nuclei ( $\alpha Z \ll 1$ ) and ultra-relativistic electrons ( $p_e \approx w$ ). After inserting the above into (2a) and (13a) we arrive at

$$\lambda_{if}^{\text{EC}} = \exp(\pi \alpha Z) \frac{\ln 2}{K} \times \int_{-q_{if}}^\infty \frac{C(w) w^2 (q_{if} + w)^2}{1 + \exp[\beta(w - \mu_e)]} dw \quad (\text{E3})$$

$$\xi_{if}^{\text{EC}} = m_e c^2 \exp(\pi \alpha Z) \frac{\ln 2}{K} \times \int_{-q_{if}}^\infty \frac{C(w) w^2 (q_{if} + w)^3}{1 + \exp[\beta(w - \mu_e)]} dw \quad (\text{E4})$$

where we have used  $\beta = 1/(kT)$ . If we then replace  $C(w)$  with the general form of a second-forbidden shape factor

(7) we get

$$\lambda_{if}^{\text{EC}} = \exp(\pi\alpha Z) \frac{\ln 2}{K} \times \left( a_{-1}I_{-1} + a_0I_0 + a_1I_1 + a_2I_2 + a_3I_3 + a_4I_4 \right) \quad (\text{E5})$$

$$\xi_{if}^{\text{EC}} = m_e c^2 \exp(\pi\alpha Z) \frac{\ln 2}{K} \times \left( a_{-1}J_{-1} + a_0J_0 + a_1J_1 + a_2J_2 + a_3J_3 + a_4J_4 \right) \quad (\text{E6})$$

where we have the integrals

$$I_n = \frac{w^{2+n}(q_{if} + w)^2}{1 + \exp[\beta(w - \mu_e)]} \quad (\text{E7})$$

$$J_n = \frac{w^{2+n}(q_{if} + w)^3}{1 + \exp[\beta(w - \mu_e)]}. \quad (\text{E8})$$

We can express  $I_n$  in terms of Fermi integrals by first introducing the quantities  $\eta = \beta\mu_e$  and  $\zeta = \beta q_{if}$  and then making the variable substitution  $x = \beta(w + q_{if})$ . The result is

$$\begin{aligned} I_{-1} &= \frac{1}{\beta^4} [F_3(\eta + \zeta) - \zeta F_2(\eta + \zeta)] \\ I_0 &= \frac{1}{\beta^5} [F_4(\eta + \zeta) - 2\zeta F_3(\eta + \zeta) + \zeta^2 F_2(\eta + \zeta)] \\ I_1 &= \frac{1}{\beta^6} [F_5(\eta + \zeta) - 3\zeta F_4(\eta + \zeta) + 3\zeta^2 F_3(\eta + \zeta) - \zeta^3 F_2(\eta + \zeta)] \\ I_2 &= \frac{1}{\beta^7} [F_6(\eta + \zeta) - 4\zeta F_5(\eta + \zeta) + 6\zeta^2 F_4(\eta + \zeta) - 4\zeta^3 F_3(\eta + \zeta) + \zeta^4 F_2(\eta + \zeta)] \\ I_3 &= \frac{1}{\beta^8} [F_7(\eta + \zeta) - 5\zeta F_6(\eta + \zeta) + 10\zeta^2 F_5(\eta + \zeta) - 10\zeta^3 F_4(\eta + \zeta) + 5\zeta^4 F_3(\eta + \zeta) - \zeta^5 F_2(\eta + \zeta)] \\ I_4 &= \frac{1}{\beta^9} [F_8(\eta + \zeta) - 6\zeta F_7(\eta + \zeta) + 15\zeta^2 F_6(\eta + \zeta) - 20\zeta^3 F_5(\eta + \zeta) + 15\zeta^4 F_4(\eta + \zeta) - 6\zeta^5 F_3(\eta + \zeta) + \zeta^6 F_2(\eta + \zeta)]. \end{aligned}$$

Applying the same approach to  $J_n$  yields

$$J_{-1} = \frac{1}{\beta^5} [F_4(\eta + \zeta) - \zeta F_3(\eta + \zeta)]$$

$$\begin{aligned} J_0 &= \frac{1}{\beta^6} [F_5(\eta + \zeta) - 2\zeta F_4(\eta + \zeta) + \zeta^2 F_3(\eta + \zeta)] \\ J_1 &= \frac{1}{\beta^7} [F_6(\eta + \zeta) - 3\zeta F_5(\eta + \zeta) + 3\zeta^2 F_4(\eta + \zeta) - \zeta^3 F_3(\eta + \zeta)] \\ J_2 &= \frac{1}{\beta^8} [F_7(\eta + \zeta) - 4\zeta F_6(\eta + \zeta) + 6\zeta^2 F_5(\eta + \zeta) - 4\zeta^3 F_4(\eta + \zeta) + \zeta^4 F_3(\eta + \zeta)] \\ J_3 &= \frac{1}{\beta^9} [F_8(\eta + \zeta) - 5\zeta F_7(\eta + \zeta) + 10\zeta^2 F_6(\eta + \zeta) - 10\zeta^3 F_5(\eta + \zeta) + 5\zeta^4 F_4(\eta + \zeta) - \zeta^5 F_3(\eta + \zeta)] \\ J_4 &= \frac{1}{\beta^{10}} [F_9(\eta + \zeta) - 6\zeta F_8(\eta + \zeta) + 15\zeta^2 F_7(\eta + \zeta) - 20\zeta^3 F_6(\eta + \zeta) + 15\zeta^4 F_5(\eta + \zeta) - 6\zeta^5 F_4(\eta + \zeta) + \zeta^6 F_3(\eta + \zeta)]. \end{aligned}$$

We have implemented the above expressions in the rate calculation routines in MESA. Note that the shape factor  $C(w)$  must be reevaluated throughout the simulation as the Coulomb correction (8a) varies with density and temperature. (This quantity enters (A2)–(A5) via the neutrino momentum  $p_\nu^{\text{EC}} = q_{if}^{\text{EC,med}} + w$ .) As a consequence we must write the coefficients  $a_{-1}, a_0 \dots a_4$  in (7) as functions of  $q_{if}^{\text{EC,med}}$  so that MESA can compute their values at each simulation step. For the  $0_{\text{g.s.}}^+ \rightarrow 2_{\text{g.s.}}^+$  transition in  $^{20}\text{Ne}(e^-, \nu_e)^{20}\text{F}$  we use the SM+CVC+E2 fit from Ref. [19], which gives us

$$\begin{aligned} a_{-1} &= (-5.191 - 0.3228q + 8.411q^2 + 0.3222q^3) \times 10^{-11} \\ a_0 &= (-659.9 - 65.33q + 624.3q^2 + 48.01q^3 + 1.009q^4) \times 10^{-11} \\ a_1 &= (-63.35 + 1248q + 135.6q^2 + 3.712q^3) \times 10^{-11} \\ a_2 &= (1283 + 209.3q + 8.446q^2) \times 10^{-11} \\ a_3 &= (116.5 + 9.469q) \times 10^{-11} \\ a_4 &= 4.734 \times 10^{-11}. \end{aligned}$$

Here we have written  $q = q_{if}^{\text{EC,med}}$  for brevity (note that  $q < 0$ ). Similarly, for the  $4_{\text{g.s.}}^+ \rightarrow 2_1^+$  transition in  $^{24}\text{Na}(e^-, \nu_e)^{24}\text{Ne}$  the coefficients in the SM+CVC shape factor are

$$\begin{aligned} a_{-1} &= (-5.690 + 10.10q - 130.7q^2 - 10.08q^3) \times 10^{-13} \\ a_0 &= (15.48 - 256.8q + 199.2q^2 + 38.81q^3 + 6.702q^4) \times 10^{-13} \\ a_1 &= (-11.47 + 40.85q + 24.76q^2 + 3.692q^3) \times 10^{-12} \\ a_2 &= (18.71 + 37.41q + 9.289q^2) \times 10^{-12} \\ a_3 &= (1.596 + 1.119q) \times 10^{-11} \\ a_4 &= 5.597 \times 10^{-12}. \end{aligned}$$

- [1] C. L. Doherty, P. Gil-Pons, L. Siess, and J. C. Lattanzio, Super-AGB Stars and their Role as Electron Capture Supernova Progenitors, *Publ. Astron. Soc. Austr.* **34**, e056 (2017).
- [2] S. Jones, R. Hirschi, K. Nomoto, T. Fischer, F. X. Timmes, F. Herwig, B. Paxton, H. Toki, T. Suzuki, G. Martínez-Pinedo, Y. H. Lam, and M. G. Bertolli, Advanced Burning Stages and Fate of 8-10  $M_{\odot}$  Stars, *Astrophys. J.* **772**, 150 (2013).
- [3] K. Takahashi, T. Yoshida, and H. Umeda, Evolution of progenitors for electron capture supernovae, *Astrophys. J.* **771**, 28 (2013).
- [4] S. Miyaji, K. Nomoto, K. Yokoi, and D. Sugimoto, Supernova triggered by electron captures, *Publ. Astron. Soc. Japan* **32**, 303 (1980).
- [5] S.-C. Leung, K. Nomoto, and T. Suzuki, Electron-capture Supernovae of Super-AGB Stars: Sensitivity on Input Physics, *Astrophys. J.* **889**, 34 (2020).
- [6] J. Isern, R. Canal, and J. Labay, The outcome of explosive ignition of ONeMg cores - Supernovae, neutron stars, or "iron" white dwarfs?, *Astrophys. J.* **372**, L83 (1991).
- [7] S. Jones, F. K. Röpkke, R. Pakmor, I. R. Seitenzahl, S. T. Ohlmann, and P. V. Edelmann, Do electron-capture supernovae make neutron stars? - First multidimensional hydrodynamic simulations of the oxygen deflagration, *Astron. & Astrophys.* **593**, A72 (2016).
- [8] K. Nomoto, Evolution of 8-10 solar mass stars toward electron capture supernovae. II-Collapse of an O+Ne+Mg core, *Astrophys. J.* **322**, 206 (1987).
- [9] S. Miyaji and K. Nomoto, On the Collapse of 8-10  $M_{\text{sun}}$  Stars Due to Electron Capture, *Astrophys. J.* **318**, 307 (1987).
- [10] R. Canal, J. Isern, and J. Labay, The quasi-static evolution of ONeMg cores - Explosive ignition densities and the collapse/explosion alternative, *Astrophys. J.* **398**, L49 (1992).
- [11] M. Hashimoto, K. Iwamoto, and K. Nomoto, Type II Supernovae from 8-10  $M_{\text{sun}}$  Asymptotic Giant Branch Stars, *Astrophys. J.* **414**, L105 (1993).
- [12] J. Gutierrez, E. Garcia-Berro, I. Iben Jr, J. Isern, J. Labay, and R. Canal, The final evolution of ONeMg electron-degenerate cores, *Astrophys. J.* **459**, 701 (1996).
- [13] J. Gutiérrez, R. Canal, and E. Garcia-Berro, The gravitational collapse of ONe electron-degenerate cores and white dwarfs: The role of Mg and C revisited, *Astron. & Astrophys.* **435**, 231 (2005).
- [14] J. Schwab, E. Quataert, and L. Bildsten, Thermal runaway during the evolution of ONeMg cores towards accretion-induced collapse, *Mon. Not. Roy. Astron. Soc.* **453**, 1910 (2015); Erratum: Thermal runaway during the evolution of ONeMg cores towards accretion-induced collapse, *Mon. Not. Roy. Astron. Soc.* **458**, 3613 (2016).
- [15] J. Schwab, L. Bildsten, and E. Quataert, The importance of Urca-process cooling in accreting ONe white dwarfs, *Mon. Not. Roy. Astron. Soc.* **472**, 3390 (2017).
- [16] T. Oda, M. Hino, K. Muto, M. Takahara, and K. Sato, Rate tables for the weak processes of sd-shell nuclei in stellar matter, *At. Data Nucl. Data Tables* **56**, 231 (1994).
- [17] M. Takahara, M. Hino, T. Oda, K. Muto, A. Wolters, P. Glaudemans, and K. Sato, Microscopic calculation of the rates of electron captures which induce the collapse of O+Ne+Mg cores, *Nucl. Phys. A* **504**, 167 (1989).
- [18] G. Martínez-Pinedo, Y. H. Lam, K. Langanke, R. G. T. Zegers, and C. Sullivan, Astrophysical weak-interaction rates for selected  $A = 20$  and  $A = 24$  nuclei, *Phys. Rev. C* **89**, 045806 (2014).
- [19] O. S. Kirsebom, M. Hukkanen, A. Kankainen, W. H. Trzaska, D. F. Strömberg, G. Martínez-Pinedo, K. Andersen, E. Bodewits, B. A. Brown, L. Canete, J. Cederkäll, T. Enqvist, T. Eronen, H. O. U. Fynbo, S. Geldhof, R. de Groote, D. G. Jenkins, A. Jokinen, P. Joshi, A. Khanam, J. Kostensalo, P. Kuusiniemi, K. Langanke, I. Moore, M. Munch, D. A. Nesterenko, J. D. Ovejas, H. Penttilä, I. Pohjalainen, M. Reponen, S. Rinta-Antila, K. Riisager, A. de Roubin, P. Schotanus, P. C. Srivastava, J. Suhonen, J. A. Swartz, O. Tengblad, M. Vilen, S. Vinals, and J. Äystö, Measurement of the  $2^+ \rightarrow 0^+$  ground-state transition in the  $\beta$  decay of  $^{20}\text{F}$ , *Phys. Rev. C* **100**, 065805 (2019).
- [20] O. S. Kirsebom, S. Jones, D. F. Strömberg, G. Martínez-Pinedo, K. Langanke, F. K. Röpkke, B. A. Brown, T. Eronen, H. O. U. Fynbo, M. Hukkanen, A. Idini, A. Jokinen, A. Kankainen, J. Kostensalo, I. Moore, H. Möller, S. T. Ohlmann, H. Penttilä, K. Riisager, S. Rinta-Antila, P. C. Srivastava, J. Suhonen, W. H. Trzaska, and J. Äystö, Discovery of an Exceptionally Strong  $\beta$ -Decay Transition of  $^{20}\text{F}$  and Implications for the Fate of Intermediate-Mass Stars, *Phys. Rev. Lett.* **123**, 262701 (2019).
- [21] H. Toki, T. Suzuki, K. Nomoto, S. Jones, and R. Hirschi, Detailed  $\beta$ -transition rates for URCA nuclear pairs in 8-10 solar-mass stars, *Phys. Rev. C* **88**, 015806 (2013).
- [22] G. M. Fuller, W. A. Fowler, and M. J. Newman, Stellar weak-interaction rates for sd-shell nuclei. I. Nuclear matrix element systematics with application to  $^{26}\text{Al}$  and selected nuclei of importance to the supernova problem, *Astrophys. J. Suppl.* **42**, 447 (1980).
- [23] H. Behrens and W. Bühring, Nuclear beta decay, *Nucl. Phys. A* **162**, 111 (1971).
- [24] H. Behrens and W. Bühring, *Electron Radial Wave Functions and Nuclear Beta-decay* (Clarendon, Oxford, 1982).
- [25] W. Bambynek, H. Behrens, M. H. Chen, B. Crasemann, M. L. Fitzpatrick, K. W. D. Ledingham, H. Genz, M. Mutterer, and R. L. Intemann, Orbital electron capture by the nucleus, *Rev. Mod. Phys.* **49**, 77 (1977); Erratum: Orbital electron capture by the nucleus, *Rev. Mod. Phys.* **49**, 961 (1977).
- [26] D. F. Strömberg, *Weak interactions in degenerate oxygen-neon cores*, *Ph.D. thesis*, Technische Universität Darmstadt (2020).
- [27] J. C. Hardy and I. Towner, Superaligned  $0^+ \rightarrow 0^+$  nuclear  $\beta$  decays: A new survey with precision tests of the conserved vector current hypothesis and the standard model, *Phys. Rev. C* **79**, 055502 (2009).
- [28] P. A. Zyla *et al.* (Particle Data Group), Review of Particle Physics, *PTEP* **2020**, 083C01 (2020).
- [29] E. Bravo and D. García-Senz, Coulomb corrections to the equation of state of nuclear statistical equilibrium matter: implications for SNIa nucleosynthesis and the accretion-induced collapse of white dwarfs, *Mon. Not. Roy. Astron. Soc.* **307**, 984 (1999).
- [30] A. Juodagalvis, K. Langanke, W. R. Hix, G. Martínez-

- Pinedo, and J. M. Sampaio, Improved estimate of electron capture rates on nuclei during stellar core collapse, *Nucl. Phys. A* **848**, 454 (2010).
- [31] N. Itoh, N. Tomizawa, M. Tamamura, S. Wanajo, and S. Nozawa, Screening corrections to the electron capture rates in dense stars by the relativistically degenerate electron liquid, *Astrophys. J.* **579**, 380 (2002).
- [32] E. Caurier and F. Nowacki, Present status of shell model techniques, *Act. Phys. Pol. B* **30**, 705 (1999).
- [33] E. Caurier, G. Martínez-Pinedo, F. Nowacki, A. Poves, and A. Zuker, The shell model as a unified view of nuclear structure, *Rev. Mod. Phys.* **77**, 427 (2005).
- [34] B. A. Brown and W. Richter, New “USD” Hamiltonians for the sd shell, *Phys. Rev. C* **74**, 034315 (2006).
- [35] I. Towner, J. Hardy, and M. Harvey, Analogue symmetry breaking in superallowed fermi  $\beta$ -decay, *Nucl. Phys. A* **284**, 269 (1977).
- [36] G. Fricke, C. Bernhardt, K. Heilig, L. Schaller, L. Schellenberg, E. Spera, and C. DeJager, Nuclear ground state charge radii from electromagnetic interactions, *At. Data Nucl. Data Tables* **60**, 177 (1995).
- [37] E. K. Warburton, Second-forbidden unique  $\beta$  decays of  $^{10}\text{Be}$ ,  $^{22}\text{Na}$ , and  $^{26}\text{Al}$ , *Phys. Rev. C* **45**, 463 (1992).
- [38] G. Martínez-Pinedo and P. Vogel, Shell Model Calculation of the  $\beta^-$  and  $\beta^+$  Partial Half-Lives of  $^{54}\text{Mn}$  and Other Unique Second Forbidden  $\beta$  Decays, *Phys. Rev. Lett.* **81**, 281 (1998).
- [39] J. T. Suhonen, Value of the Axial-Vector Coupling Strength in  $\beta$  and  $\beta\beta$  Decays: A Review, *Front. Phys.* **5**, 55 (2017).
- [40] B. Singh, J. Rodriguez, S. Wong, and J. Tuli, Review Of  $\log ft$  Values In  $\beta$  Decay, *Nucl. Data Sheets* **84**, 487 (1998).
- [41] R. B. Firestone, Nuclear data sheets for A=24, *Nucl. Data Sheets* **108**, 2319 (2007).
- [42] J. F. Turner and P. E. Cavanagh, Highly forbidden transitions in the decay of  $\text{Na}^{24}$ , *Philos. Mag.* **42**, 636 (1951).
- [43] M. S. Antony, A. Pape, and J. Britz, Coulomb displacement energies between analog levels for  $3 \leq A \leq 239$ , *At. Data Nucl. Data Tables* **66**, 1 (1997).
- [44] M. S. Basunia, Nuclear data sheets for A=27, *Nucl. Data Sheets* **112**, 1875 (2011).
- [45] B. Paxton, L. Bildsten, A. Dotter, F. Herwig, P. Lesaffre, and F. Timmes, Modules for experiments in stellar astrophysics (MESA), *Astrophys. J. Suppl.* **192**, 3 (2010).
- [46] W. M. Wolf, L. Bildsten, J. Brooks, and B. Paxton, Hydrogen burning on accreting white dwarfs: stability, recurrent novae, and the post-nova supersoft phase, *Astrophys. J.* **777**, 136 (2013).
- [47] J. Brooks, L. Bildsten, J. Schwab, and B. Paxton, Carbon Shell or Core Ignitions in White Dwarfs Accreting from Helium Stars, *Astrophys. J.* **821**, 28 (2016).
- [48] J. Schwab and K. A. Rocha, Residual Carbon in Oxygen–Neon White Dwarfs and Its Implications for Accretion-induced Collapse, *Astrophys. J.* **872**, 131 (2019).
- [49] H. A. Weidenmüller, First-Forbidden Beta Decay, *Rev. Mod. Phys.* **33**, 574 (1961).
- [50] L. C. Biedenharn and M. E. Rose, Theory of Angular Correlation of Nuclear Radiations, *Rev. Mod. Phys.* **25**, 729 (1953).
- [51] E. U. Condon and G. Shortley, *The Theory of Atomic Spectra* (Cambridge University Press, Cambridge, England, 1951).
- [52] R. A. Ward and W. A. Fowler, Thermalization of long-lived nuclear isomeric states under stellar conditions, *Astrophys. J.* **238**, 266 (1980).
- [53] B. Paxton, P. Marchant, J. Schwab, E. B. Bauer, L. Bildsten, M. Cantiello, L. Dessart, R. Farmer, H. Hu, N. Langer, *et al.*, Modules for experiments in stellar astrophysics (MESA): binaries, pulsations, and explosions, *Astrophys. J. Suppl.* **220**, 15 (2015); Erratum: “Modules for experiments in stellar astrophysics (MESA): binaries, pulsations, and explosions”, *Astrophys. J. Suppl.* **223**, 18 (2016).